J. Fluid Mech. (2026), *vol.* 1034, A59, doi:10.1017/jfm.2026.11543

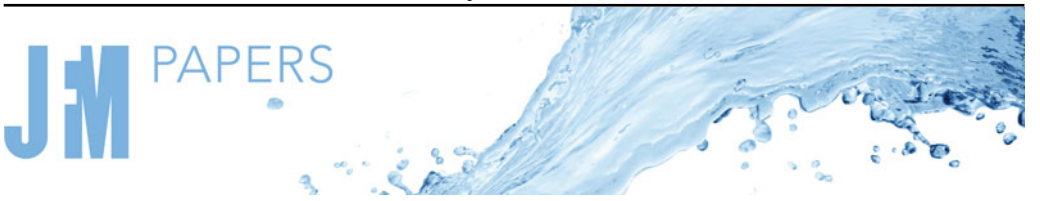

Dispersion of active particles in oscillatory Poiseuille flow

Vhaskar Chakraborty[1], **Pankaj Mishra**[1], **Mingfeng Qiu**[2] **and Zhiwei Peng**[3]

[1]Department of Physics, Indian Institute of Technology (ISM), Dhanbad 826004, India

[2]School of Mathematics and Statistics, University of Canterbury, Christchurch 8140, New Zealand

[3]Department of Chemical and Materials Engineering, University of Alberta, Edmonton, AB T6G 1H9, Canada

Corresponding author: Zhiwei Peng, zhiwei.peng@ualberta.ca

(Received 22 July 2025; revised 17 March 2026; accepted 14 April 2026)

Active particles exhibit complex transport dynamics in flows through confined geometries such as channels or pores. In this work, we employ a generalised Taylor dispersion (GTD) theory to study the long-time dispersion behaviour of active Brownian particles in an oscillatory Poiseuille flow within a planar channel. We quantify the time-averaged longitudinal dispersion coefficient as a function of the flow speed, flow oscillation frequency and particle activity. In the weak-activity limit, asymptotic analysis shows that activity can either enhance or hinder the dispersion compared with the passive case. For arbitrary activity levels, we numerically solve the GTD equations and validate the results with Brownian dynamics simulations. We show that the dispersion coefficient can vary non-monotonically with both the flow speed and particle activity. Furthermore, the dispersion coefficient shows an oscillatory behaviour as a function of the flow oscillation frequency, exhibiting distinct minima and maxima at different frequencies. The observed oscillatory dispersion results from the interplay between self-propulsion and oscillatory flow advection – a coupling absent in passive or steady systems. Our results show that time-dependent flows can be used to tune the dispersion of active particles in confinement.

Key words: active matter, colloids, dispersion

1. Introduction

For micron-sized particles, the presence of fluid flow can enhance mass transport due to the interplay between advection and diffusion. A classical example of this coupling effect is Taylor dispersion, where Brownian solutes in pressure-driven flows exhibit enhanced

longitudinal dispersion compared with the molecular diffusivity (Taylor 1953, 1954*a*,*b*; Aris 1956). Since the work of Taylor (1953), a generalised Taylor dispersion (GTD) framework has been developed to study a variety of transport phenomena. These include complex geometries, spatial and temporal periodicity and active (i.e. self-propelled) particle dynamics (Brenner 1980; Shapiro & Brenner 1990; Hill & Bees 2002; Zia & Brady 2010; Brenner 2013; Alonso-Matilla, Chakrabarti & Saintillan 2019; Peng & Brady 2020; Peng 2024).

Active particles differ from passive solutes in that each unit is capable of self-propulsion (Schweitzer, Ebeling & Tilch 1998; Romanczuk *et al.* 2012). The interplay between self-propulsion and fluid flow gives rise to a rich and often non-intuitive dynamics that is absent in passive Brownian systems (Romanczuk *et al.* 2012; Bechinger *et al.* 2016; Gomez-Solano, Blokhuis & Bechinger 2016; Chandragiri *et al.* 2020; Jing *et al.* 2020; Plan *et al.* 2020; Chakraborty *et al.* 2022; Choudhary *et al.* 2022). One example where this dynamics plays a crucial role is the transport behaviour of microswimmers, which is important for understanding both natural and engineered systems, such as infection by motile bacteria (Siitonen & Nurminen 1992; Lane *et al.* 2005), formation of biofilms (Rusconi *et al.* 2010; Kim *et al.* 2014), drug delivery (Park *et al.* 2017; Díez *et al.* 2021; Lin *et al.* 2021; Sridhar *et al.* 2022), therapeutic treatments (Ghosh *et al.* 2020) and environmental remediation (Soler *et al.* 2013; Urso, Ussia & Pumera 2023).

Transport of active particles often occurs in confined geometries, where Poiseuille flow is a common flow profile, and considerable work has focused on how active matter behaves in such environments (Zöttl & Stark 2012, 2013; Apaza & Sandoval 2016; Junot *et al.* 2019; Mathijssen *et al.* 2019; Anand & Singh 2021; Chuphal, Sahoo & Thakur 2021; Choudhary *et al.* 2022; Khatri & Burada 2022; Walker *et al.* 2022; Ganesh *et al.* 2023; Valani, Harding & Stokes 2024). For instance, in channels, active particles exhibit upstream swimming in Poiseuille flow (Kaya & Koser 2012; Kantsler *et al.* 2014; Ezhilan & Saintillan 2015; Omori & Ishikawa 2016). Owing to their upstream motility, *Escherichia coli* introduced downstream causes upstream contamination in initially clean microfluidic channels (Figueroa-Morales *et al.* 2020). Further investigations by Mathijssen *et al.* (2019) on bacterial motion near channel surfaces revealed that *E. coli* engages in distinct rheotaxis regimes depending on the shear rate. With increasing shear, the bacteria transition from upstream swimming to oscillatory rheotaxis, and ultimately to a coexistence of rheotaxis aligned with both positive and negative vorticity directions.

While these studies were primarily focused on steady flows, biologically relevant systems are often governed by time-dependent flow conditions. McDonald (1955) experimentally studied the relationship between pulsatile pressure and blood flow in arteries, analysing the phasic variations in arterial flow during each cardiac cycle. Inspired by the study of McDonald (1955), Womersley (1955) investigated the velocity, rate of flow and viscous drag in arteries by considering a time-periodic pressure gradient. The primary factors governing such flows include the pulsatile pressure generated by the heart, the structural and mechanical properties of the vascular walls and the flow behaviour of blood (Secomb 2016).

Early studies on longitudinal dispersion of passive contaminants in oscillatory pressure-driven flows were carried out by Chatwin (1975, 1977). Later, Watson (1983) derived analytical solutions for the long-time effective dispersivity in oscillatory flows within both pipes and rectangular channels. His results showed that the effective dispersivity decreases monotonically with increasing flow frequency. Subsequently, Mazumder & Das (1992) investigated how boundary absorption and heterogeneous reactions influence contaminant dispersion in both steady and oscillatory flows. The significance of such boundary interactions lies in their relevance to processes such as deposition and transport across

semi-permeable membranes. More recently, Chu *et al.* (2019) developed a macro-transport theory for two-dimensional flows in a parallel plate channel with alternating shear-free and no-slip regions. They considered both steady and oscillatory flow components to study the transport coefficients of passive particles. Later, they extended their analysis to eccentric annuli (Chu *et al.* 2020) where they showed that the maximum dispersion observed in a time-oscillatory flow can be achieved by applying a slowly oscillating flow in an annulus with large eccentricity. Hettiarachchi *et al.* (2011) used experiments and simulations to show that pulsatile cerebrospinal fluid significantly enhances drug dispersion in the spinal cord relative to no flow.

Although the dispersion of passive particles in oscillatory flows has been widely studied, much less is known about the transport of microswimmers in oscillatory flows. Recently, using experiments and simulations, Caldag & Bees (2025) showed that oscillatory flow can lead to a non-trivial dispersion dynamics in gyrotactic swimmers. Wang *et al.* (2025) studied Taylor–Aris dispersion of active particles in oscillatory channel flows and showed that spherical non-gyrotactic swimmers can exhibit either enhanced or reduced diffusivity relative to passive solutes due to disruption of cross-streamline migration associated with Jeffery orbits. Lagoin *et al.* (2025) experimentally investigated the motility and dispersion of *Chlamydomonas reinhardtii* microalgae within a rectangular microfluidic channel under sinusoidal Poiseuille flow, showing that velocity fluctuations and the dispersion coefficient increase with flow amplitude, with weak dependencies on flow periodicity. In this paper, we consider the dispersion of active Brownian particles (ABPs) in time-periodic pressure-driven Poiseuille flow through planar channels. We apply the GTD theory of Peng & Brady (2020), originally developed for ABPs in steady flow, to characterise the long-time longitudinal dispersion of ABPs in oscillatory flow. Due to the time-periodic nature of the flow, an additional time average over one oscillation period is performed to define the time-averaged dispersion coefficient (Chatwin 1975, 1977; Watson 1983). In the weak-swimming limit, characterised by a small swim Péclet number ($Pe_s \ll 1$), we show that the first effect of swimming on longitudinal dispersion appears at $O(Pe_s^2)$. Depending on the flow Péclet number (Pe) and oscillation frequency, the $O(Pe_s^2)$ contribution can be either positive or negative. As such, activity can either enhance or hinder longitudinal dispersion in oscillatory Poiseuille flow compared with passive Brownian particles. For arbitrary swim speeds, numerical solutions of the governing equations are used to characterise the dispersion as a function of the flow speed, swim speed and oscillation frequency. Numerical results are validated against Brownian dynamics (BD) simulations.

2. Problem formulation

2.1. *The Smoluchowski equation*

We consider the long-time transport behaviour of ABPs dispersed in a viscous Newtonian solvent confined between two parallel plates with a separation distance of $2H$. In the dilute limit, we only consider the dynamics of a single ABP. The ABP is assumed to be spherical, and its radius is much smaller than the width of the channel. This allows us to treat the ABP as a 'point' particle. An ABP self-propels with a constant swim speed U_s in a body-fixed swimming direction $\boldsymbol{q}$ ($\boldsymbol{q} \cdot \boldsymbol{q} = 1$). Due to rotational Brownian motion, the orientation vector $\boldsymbol{q}$ undergoes stochastic reorientation. The configuration of an ABP at time t is described by its position vector $\boldsymbol{x}$ and by the orientation vector $\boldsymbol{q}$. We define $P(\boldsymbol{x}, \boldsymbol{q}, t)$ as the probability density function of finding the ABP at position $\boldsymbol{x}$ with orientation $\boldsymbol{q}$ at time t. It satisfies the Smoluchowski equation

$$\frac{\partial P}{\partial t} + \nabla \cdot \boldsymbol{j}_T + \nabla_R \cdot \boldsymbol{j}_R = 0, \tag{2.1}$$

where $\boldsymbol{\nabla} = \partial/\partial \boldsymbol{x}$ and $\boldsymbol{\nabla}_R = \boldsymbol{q} \times \partial/\partial \boldsymbol{q}$ are the spatial and rotational gradient operators, respectively. In (2.1),

$$\boldsymbol{j}_T = U_s \boldsymbol{q} P + \boldsymbol{u}_f P - D_T \boldsymbol{\nabla} P, \tag{2.2}$$

$$\boldsymbol{j}_R = \boldsymbol{\Omega}_f P - D_R \boldsymbol{\nabla}_R P, \tag{2.3}$$

where $\boldsymbol{u}_f$ is the background fluid velocity field, D_T is the translational diffusivity of the ABP, $\boldsymbol{\Omega}_f = (1/2)\boldsymbol{\nabla} \times \boldsymbol{u}_f$ is the flow-induced angular velocity and D_R is the rotational diffusivity of the ABP. The inverse of D_R, $\tau_R = 1/D_R$, defines the reorientation time. At the channel walls, the no-flux boundary condition is satisfied (Ezhilan & Saintillan 2015; Peng & Brady 2020)

$$\boldsymbol{e}_y \cdot \boldsymbol{j}_T = 0, \quad y = \pm H, \tag{2.4}$$

where $\boldsymbol{e}_y$ is the unit normal to the channel walls. The longitudinal Cartesian coordinate is x and y is the transverse coordinate.

2.2. *Oscillatory Poiseuille flow*

For ease of reference, we provide a brief outline of the flow field derivation. We consider a one-dimensional flow, $\boldsymbol{u}_f = u(y, t)\boldsymbol{e}_x$, driven by a prescribed oscillatory pressure gradient along the channel (Womersley 1955). Here, $\boldsymbol{e}_x$ is the unit basis vector in the longitudinal direction. The Navier–Stokes equations reduce to

$$\rho \frac{\partial u}{\partial t} = -\frac{\partial p}{\partial x} + \mu \frac{\partial^2 u}{\partial y^2}, \tag{2.5}$$

where ρ is the density of the fluid, μ is the dynamic viscosity of the fluid and the prescribed pressure gradient is given by

$$-\frac{\partial p}{\partial x} = \frac{P_0}{H} \cos(\omega t). \tag{2.6}$$

In (2.6), P_0 is a reference pressure and ω is the angular frequency of the actuation. One can show that the solution of (2.5) may be written as $u(y, t) = \mathrm{Re}[u'(y)e^{i\omega t}]$, where

$$u'(y) = \frac{i P_0}{\rho H \omega} \left[-1 + \cosh\left((1+i)\lambda y\right) \operatorname{sech}\left((1+i)\lambda H\right)\right]. \tag{2.7}$$

In (2.7), $i = \sqrt{-1}$ is the imaginary unit, $\nu = \mu/\rho$ is the kinematic viscosity of the fluid and $\lambda = \sqrt{\omega/(2\nu)}$. The viscous length, $1/\lambda = \sqrt{2\nu/\omega}$, sets the scale over which the fluid momentum diffuses during one oscillation cycle of the applied pressure. The operator Re extracts the real part of a complex quantity.

In the zero-frequency limit, $\omega \to 0$, we recover the steady Poiseuille flow as

$$u(y, t) \to \frac{P_0 H}{2\mu} \left(1 - \frac{y^2}{H^2}\right). \tag{2.8}$$

For convenience, we define the characteristic flow speed $U_f = P_0 H/(2\mu)$. Using this, we rewrite (2.7) as

$$u'(y) = \frac{i U_f}{(\lambda H)^2} \left[-1 + \cosh\left((1+i)\lambda y\right) \operatorname{sech}\left((1+i)\lambda H\right)\right]. \tag{2.9}$$

The angular velocity $\Omega_f(y,t) = \mathrm{Re}[\Omega' e^{i\omega t}]$, where

$$\Omega' = -\frac{1}{2}\frac{\partial u'}{\partial y} = \frac{(1-i)U_f}{2\lambda H^2}\sinh((1+i)\lambda y)\,\mathrm{sech}\,((1+i)\lambda H). \tag{2.10}$$

2.3. *Generalised Taylor dispersion theory*

Taking the zeroth orientational moment of (2.1) gives the governing equation for the number density

$$\frac{\partial n}{\partial t} + \boldsymbol{\nabla}\cdot\left(\boldsymbol{u}_f n + U_s \boldsymbol{m} - D_T \boldsymbol{\nabla} n\right) = 0, \tag{2.11}$$

where $n = \int_{\mathbb{S}} P \mathrm{d}\boldsymbol{q}$ is the number density, and $\boldsymbol{m} = \int_{\mathbb{S}} \boldsymbol{q} P \mathrm{d}\boldsymbol{q}$ is the first moment, or polar order. Here, $\mathbb{S} = \{\boldsymbol{q} \mid \boldsymbol{q}\cdot\boldsymbol{q} = 1\}$ denotes the unit sphere of orientations. In the following, we present a general derivation and then specialise to two dimensions. Since the channel is unbounded in the x direction, it is convenient to work in Fourier space. To derive a long-time effective transport equation, we first define the Fourier transform of a function $f(x)$ as $\hat{f}(k) = \int e^{-ikx} f(x)\mathrm{d}x$, where k is the wavenumber. Following Peng & Brady (2020), one can show that

$$\frac{\partial \overline{n}}{\partial t} + k^2 D_T \overline{n} + ik\left(\overline{u(y,t)\hat{n}} + U_s \overline{\hat{m}_x}\right) = 0, \tag{2.12}$$

where we have made use of the no-flux condition, and an overhead bar denotes the cross-sectional average

$$\overline{n}(k,t) = \frac{1}{2H}\int_{-H}^{H} \hat{n}(k,y,t)\mathrm{d}y. \tag{2.13}$$

In (2.12), $\hat{m}_x = \boldsymbol{e}_x\cdot\hat{\boldsymbol{m}}$ is the polar order in the x direction in Fourier space.

Introducing the non-dimensional density or structure function $\hat{G}$ such that $\hat{P}(k,y,\boldsymbol{q},t) = \overline{n}(k,t)\hat{G}(k,y,\boldsymbol{q},t)$ and the small-wavenumber expansion $\hat{G} = g(y,\boldsymbol{q},t) + ik\,b(y,\boldsymbol{q},t) + O(k^2)$, we obtain

$$\frac{\partial \overline{n}}{\partial t} + ikU^{eff}\overline{n} + k^2 D^{eff}\overline{n} + O(k^3) = 0, \tag{2.14}$$

where the effective drift and the effective longitudinal dispersivity are given by, respectively,

$$U^{eff} = U^{eff}(t) = U_s\overline{m_x^0} + \overline{un^0}, \tag{2.15}$$

$$D^{eff} = D^{eff}(t) = D_T - U_s\overline{\tilde{m}_x} - \overline{u\tilde{n}}. \tag{2.16}$$

In the small-wavenumber expansion, g is the average field and b is the displacement (or fluctuating) field. Note that b has units of length, e.g. displacement. We emphasise that terms of order k^3 and higher do not contribute to either the drift or the dispersion coefficient, as evidenced in (2.14). In general, a diffusive flux is proportional to the gradient of a concentration; equivalently, in a small-wavenumber expansion in Fourier space, it appears at second order in k. Physically, a diffusivity describes only leading-order gradient transport and therefore cannot capture higher-order effects. Likewise, drift and diffusivity characterise only the lowest moments of the underlying probability distribution. To resolve the full probability distribution, one must retain higher-order moments.

The orientational moments in (2.15) are given by

$$n^0 = \int_{\mathbb{S}} g \mathrm{d}\boldsymbol{q}, \quad \text{and} \quad \boldsymbol{m}^0 = \int_{\mathbb{S}} \boldsymbol{q} g \mathrm{d}\boldsymbol{q}. \tag{2.17}$$

Similarly, in (2.16), we have

$$\tilde{n} = \int_{\mathbb{S}} b \mathrm{d}\boldsymbol{q}, \quad \text{and} \quad \tilde{\boldsymbol{m}} = \int_{\mathbb{S}} \boldsymbol{q} b \mathrm{d}\boldsymbol{q}. \tag{2.18}$$

Different from the constant transport coefficients in Peng & Brady (2020), the long-time transport coefficients in (2.15) and (2.16) are time-dependent due to the oscillatory flow.

The governing equations and boundary conditions for g and b are derived in Peng & Brady (2020). For the average field, we have

$$\frac{\partial g}{\partial t} + \frac{\partial}{\partial y}\left(U_s q_y g - D_T \frac{\partial g}{\partial y}\right) + \nabla_R \cdot \left(\boldsymbol{\Omega}_f g - D_R \nabla_R g\right) = 0, \tag{2.19}$$

and

$$U_s q_y g - D_T \frac{\partial g}{\partial y} = 0, \quad y = \pm H. \tag{2.20}$$

The displacement field is governed by

$$\frac{\partial b}{\partial t} + \frac{\partial}{\partial y}\left(U_s q_y b - D_T \frac{\partial b}{\partial y}\right) + \nabla_R \cdot \left(\boldsymbol{\Omega}_f b - D_R \nabla_R b\right) = \left(U^{eff} - u - U_s q_x\right) g, \tag{2.21}$$

$$U_s q_y b - D_T \frac{\partial b}{\partial y} = 0, \quad y = \pm H. \tag{2.22}$$

Noting that

$$\frac{1}{2H} \int_{-H}^{H} \mathrm{d}y \int_{\mathbb{S}} \hat{G} \mathrm{d}\boldsymbol{q} = 1, \tag{2.23}$$

we have

$$\frac{1}{2H} \int_{-H}^{H} \mathrm{d}y \int_{\mathbb{S}} g \mathrm{d}\boldsymbol{q} = 1, \quad \text{and} \quad \frac{1}{2H} \int_{-H}^{H} \mathrm{d}y \int_{\mathbb{S}} b \mathrm{d}\boldsymbol{q} = 0. \tag{2.24}$$

The above derivation of the GTD theory applies in both two and three dimensions. In the remainder of the paper, we restrict attention to two dimensions, where the orientation vector is parametrised as $\boldsymbol{q} = \cos\phi\, \boldsymbol{e}_x + \sin\phi\, \boldsymbol{e}_y$, with $\phi \in [0, 2\pi)$ being the orientation angle. In two dimensions, the rotational gradient operator is given by $\nabla_R = \boldsymbol{e}_z(\partial/\partial\phi)$, where $\boldsymbol{e}_z = \boldsymbol{e}_x \times \boldsymbol{e}_y$.

2.4. *Non-dimensionalisation*

We scale lengths with the channel half-width H and time with the reorientation time τ_R. The system is governed by five non-dimensional parameters

$$Pe = \frac{U_f \tau_R}{H}, \quad Pe_s = \frac{U_s \tau_R}{H} = \frac{\ell}{H}, \quad \gamma = \frac{\sqrt{D_T \tau_R}}{H} = \frac{\delta}{H}, \tag{2.25a}$$

$$\chi = \omega\, \tau_R, \quad \kappa = \lambda H = \sqrt{\omega/(2\nu)}\, H, \tag{2.25b}$$

where Pe is the flow Péclet number that compares the reorientation time τ_R with the flow time scale H/U_f, Pe_s is the swim Péclet number that compares the reorientation time with

the swim time scale H/U_s, γ is a non-dimensional measure of the microscopic length $\delta = \sqrt{D_T \tau_R}$, χ is the non-dimensional flow frequency and κ compares the length scale $1/\lambda$ with the channel half-width H. The microscopic length δ characterises the distance a particle travels by translational diffusion over the time scale defined by τ_R. The swim Péclet number can be viewed as a comparison between the persistence length (or run length), $\ell = U_s \tau_R$, and the channel half-width.

Since both χ and κ contains ω, it is useful to introduce the non-dimensional parameter

$$\alpha = \frac{\chi}{\kappa^2} = \frac{2\nu\tau_R}{H^2}, \tag{2.26}$$

when analysing the effect of flow frequency ω on dispersion behaviour. With this, varying the dimensional frequency ω corresponds to changing χ while keeping α constant. To estimate the order of magnitude of α in realistic systems, consider motile bacteria such as *E. coli* in water at room temperature. Taking $H \sim 100\,\mu\text{m}$, $\tau_R \sim 1$ s (Berg & Brown 1972; Berg 2004) and $\nu \sim 10^{-6}\,\text{m}^2\,\text{s}^{-1}$, we have $\alpha \sim 10^2$. For narrower microfluidic channels, α would be even larger. For bacteria or synthetic active particles with a shorter reorientation time, α is smaller. In the remainder of the paper, we take $\alpha = 100$ unless stated otherwise.

The non-dimensional form of (2.19) is

$$\frac{\partial g}{\partial t^*} + \frac{\partial}{\partial y^*}\left(Pe_s q_y g - \gamma^2 \frac{\partial g}{\partial y^*}\right) + \frac{\partial}{\partial \phi}\left(\Omega_f^* g - \frac{\partial g}{\partial \phi}\right) = 0, \tag{2.27}$$

where we have used the parametrisation $\boldsymbol{q} = \cos\phi\, \boldsymbol{e}_x + \sin\phi\, \boldsymbol{e}_y$ with $\phi \in [0, 2\pi)$ being the orientation angle, $y^* \in [-1, 1]$, and we have used the superscript '$*$' to denote dimensionless quantities. That is, $t^* = t/\tau_R$, $y^* = y/H$ and $\Omega_f^* = \Omega_f \tau_R = \text{Re}[\Omega'^* e^{i\chi t^*}]$, where

$$\Omega'^* = \Omega' \tau_R = \frac{(1-i)Pe}{2\kappa} \sinh\left((1+i)\kappa y^*\right) \text{sech}\left((1+i)\kappa\right). \tag{2.28}$$

The superscript on g is suppressed since g is non-dimensional. With the solution of g, we can obtain the non-dimensional drift via

$$U^{eff*}(t^*) = U^{eff}\tau_R/H = Pe_s \overline{m_x^0} + \overline{u^* n^0}. \tag{2.29}$$

Similarly, we may write the non-dimensional form of (2.21) as

$$\frac{\partial b^*}{\partial t^*} + \frac{\partial}{\partial y^*}\left(Pe_s q_y b^* - \gamma^2 \frac{\partial b^*}{\partial y^*}\right) + \frac{\partial}{\partial \phi}\left(\Omega_f^* b^* - \frac{\partial b^*}{\partial \phi}\right) = \left(U^{eff*} - u^* - Pe_s q_x\right) g, \tag{2.30}$$

where $b^* = b/H$ and $u^* = u\tau_R/H = \text{Re}[u'^* e^{i\chi t^*}]$. The complex flow amplitude is given by

$$u'^* = \frac{iPe}{\kappa^2}\left[-1 + \cosh\left((1+i)\kappa y^*\right) \text{sech}\left((1+i)\kappa\right)\right]. \tag{2.31}$$

To characterise the dispersion of active particles in an oscillatory Poiseuille flow, we compare the effective dispersion coefficient with the translational diffusivity. Using (2.16), we have

$$D^{eff*} = \frac{D^{eff}}{D_T} = 1 - \frac{Pe_s}{\gamma^2}\overline{\tilde{m}_x^*} - \frac{1}{\gamma^2}\overline{u^* \tilde{n}^*}. \tag{2.32}$$

If $Pe = 0$, or $U_f = 0$, the problem reduces to that of diffusion of ABPs in a flat channel without flow. In this case, we have $D^{eff} = D_{nf}^{eff} = D_T + D^{swim}$, where $D^{swim} = U_s^2 \tau_R/2$

in two-dimensions (Berg 1993), and D_{nf}^{eff} is the effective dispersivity without flow. In non-dimensional form, we have

$$\frac{D_{nf}^{eff}}{D_T} = 1 + \frac{Pe_s^2}{2\gamma^2}. \tag{2.33}$$

For an oscillatory Poiseuille flow, D^{eff} after the initial transients becomes a periodic function of time. At long times, we define the time-averaged effective dispersion coefficient as

$$\langle D^{eff*} \rangle = \lim_{t' \to \infty} \frac{1}{T} \int_{t'}^{t'+T} D^{eff*}(t^*) \mathrm{d}t^*, \tag{2.34}$$

where $T = 2\pi/\chi$ is the period of the flow oscillation. Similarly, one can define the time-averaged effective drift as $\langle U^{eff*} \rangle$.

3. Weak-swimming asymptotic analysis

In the weak-swimming limit, characterised by $Pe_s \ll 1$, we pose regular expansions for the fields and transport coefficients

$$g = g_0 + Pe_s\, g_1 + Pe_s^2\, g_2 + \cdots, \tag{3.1}$$

$$b^* = b_0^* + Pe_s\, b_1^* + Pe_s^2\, b_2^* + \cdots, \tag{3.2}$$

$$U^{eff*} = U_0^{eff*} + Pe_s\, U_1^{eff*} + Pe_s^2\, U_2^{eff*} + \cdots, \tag{3.3}$$

$$D^{eff*} = D_0^{eff*} + Pe_s\, D_1^{eff*} + Pe_s^2\, D_2^{eff*} + \cdots. \tag{3.4}$$

3.1. *Passive Brownian particles*

At $O(1)$, the particle is passive and the average field is given by $g_0 \equiv 1/(2\pi)$. This means that the number density across the channel is uniform. As a result, the effective drift at $O(1)$ is given by $U_0^{eff*} = \overline{u^*}$, which vanishes upon time averaging.

The displacement field at $O(1)$ admits a solution of the form $b_0^* = \mathrm{Re}[A_0'(y^*)e^{i\chi t^*}/(2\pi)]$, where the solution to A_0' is provided in Appendix A. The instantaneous effective dispersion coefficient at $O(1)$ after initial transients is given by

$$D_0^{eff*}(t^*) = 1 - \frac{1}{2\gamma^2} \int_{-1}^{1} u^* \mathrm{Re}\left[A_0' e^{i\chi t^*}\right] \mathrm{d}y^*. \tag{3.5}$$

An analytical expression for the effective dispersion coefficient was derived by Watson (1983), given by

$$\langle D_0^{eff*} \rangle = 1 + \frac{Pe^2}{\kappa^2} \frac{\cosh(2\kappa) - \cos(2\kappa)}{\cosh(2\kappa) + \cos(2\kappa)} \frac{\iota(2\kappa) - \iota(\sqrt{2\chi}/\gamma)}{\chi^2 - 4\gamma^4\kappa^4}, \tag{3.6}$$

where

$$\iota(a) = \frac{\sinh(a) - \sin(a)}{a\,(\cosh(a) - \cos(a))}. \tag{3.7}$$

In figure 1, we plot the passive dispersivity ($\langle D_0^{eff} \rangle / D_T$), given in (3.6), as a function of χ and Pe. Since α is held fixed, increasing χ corresponds to increasing the dimensional

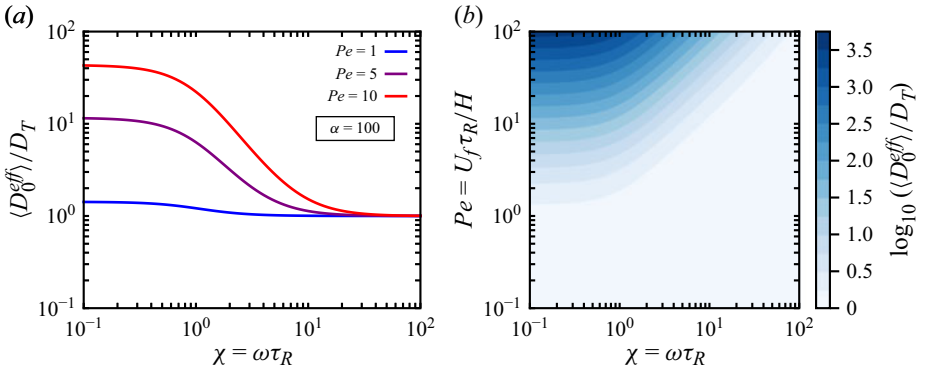

Figure 1. (*a*) Plots of the non-dimensional time-averaged effective dispersivity ($\langle D_0^{eff}\rangle/D_T$) as a function of χ. (*b*) Contour plot of the logarithm of $\langle D_0^{eff}\rangle/D_T$ as a function of Pe and χ. For all results shown, $\alpha = 100$ and $\gamma^2 = 0.1$.

frequency. In the low-frequency limit, we have $\langle D_0^{eff}\rangle/D_T \to 1 + 4Pe^2/(945\gamma^4)$ as $\chi \to 0$. For a steady Poiseuille flow of the same amplitude, the long-time dispersion coefficient $D_0^{eff}/D_T = 1 + 8Pe^2/(945\gamma^4)$. As is well known, in oscillatory flow, $(\langle D_0^{eff}\rangle - D_T)/D_T$ approaches half of its steady value as $\chi \to 0$ (Aris 1960; Bowden 1965; Van den Broeck 1982; Watson 1983; Ng 2006; Chu *et al.* 2019, 2020). On the other hand, as $\chi \to \infty$, $\langle D_0^{eff}\rangle/D_T \to 1$ regardless of Pe (see figure 1*a*). In this high-frequency limit, shear-induced dispersion vanishes due to the rapid flow oscillations. For low and intermediate frequencies, $\langle D_0^{eff}\rangle$ increases with Pe, as is consistent with Taylor dispersion. Overall, $\langle D_0^{eff}\rangle$ decreases monotonically with increasing frequency until it reaches the high-frequency limit. In figure 1(*b*), we plot the same analytical expression given in (3.6) in a contour plot as a function of both χ and Pe.

3.2. *First order*

At $O(Pe_s)$, the average field is governed by

$$\frac{\partial g_1}{\partial t^*} + \frac{\partial}{\partial y^*}\left(-\gamma^2\frac{\partial g_1}{\partial y^*}\right) + \frac{\partial}{\partial \phi}\left(\Omega_f^* g_1 - \frac{\partial g_1}{\partial \phi}\right) = -q_y\frac{\partial g_0}{\partial y^*}, \tag{3.8a}$$

$$\gamma^2\frac{\partial g_1}{\partial y^*} = q_y g_0, \quad \text{at} \quad y^* = \pm 1, \tag{3.8b}$$

$$\int_{-1}^{1} \mathrm{d}y^* \int_{\mathbb{S}} g_1 \mathrm{d}\boldsymbol{q} = 0. \tag{3.8c}$$

Assuming a solution of the form $g_1 = A_1(y^*, t^*)\cos\phi + B_1(y^*, t^*)\sin\phi$, we obtain

$$\frac{\partial A_1}{\partial t^*} - \gamma^2\frac{\partial^2 A_1}{\partial y^{*2}} + \Omega_f^* B_1 + A_1 = 0, \tag{3.9a}$$

$$\frac{\partial B_1}{\partial t^*} - \gamma^2\frac{\partial^2 B_1}{\partial y^{*2}} - \Omega_f^* A_1 + B_1 = 0, \tag{3.9b}$$

$$\frac{\partial A_1}{\partial y^*} = 0, \quad \text{and} \quad \frac{\partial B_1}{\partial y^*} = \frac{1}{2\pi\gamma^2}, \quad \text{at} \quad y^* = \pm 1. \tag{3.9c}$$

The instantaneous effective drift at this order U_1^{eff*} vanishes.

The displacement field at $O(Pe_s)$ is governed by

$$\frac{\partial b_1^*}{\partial t^*} + \frac{\partial}{\partial y^*}\left(-\gamma^2\frac{\partial b_1^*}{\partial y^*}\right) + \frac{\partial}{\partial \phi}\left(\Omega_f^* b_1^* - \frac{\partial b_1^*}{\partial \phi}\right) = -q_y\frac{\partial b_0^*}{\partial y^*} + \left(U_0^{eff*} - u^*\right)g_1 + \left(U_1^{eff*} - q_x\right)g_0, \tag{3.10a}$$

$$\gamma^2\frac{\partial b_1^*}{\partial y^*} = q_y b_0^*, \quad \text{at} \quad y^* = \pm 1, \tag{3.10b}$$

$$\int_{-1}^{1} \mathrm{d}y^* \int_{\mathbb{S}} b_1^* \mathrm{d}\boldsymbol{q} = 0, \tag{3.10c}$$

which admits a solution of the form $b_1^* = A_2(y^*, t^*)\cos\phi + B_2(y^*, t^*)\sin\phi$. Inserting this form into (3.10), we obtain

$$\frac{\partial A_2}{\partial t^*} - \gamma^2\frac{\partial^2 A_2}{\partial y^{*2}} + \Omega_f^* B_2 + A_2 = \left(U_0^{eff*} - u^*\right)A_1 - g_0, \tag{3.11a}$$

$$\frac{\partial B_2}{\partial t^*} - \gamma^2\frac{\partial^2 B_2}{\partial y^{*2}} - \Omega_f^* A_2 + B_2 = -\frac{\partial b_0^*}{\partial y^*} + \left(U_0^{eff*} - u^*\right)B_1, \tag{3.11b}$$

$$\frac{\partial A_2}{\partial y^*} = 0, \quad \text{and} \quad \frac{\partial B_2}{\partial y^*} = \frac{b_0^*}{\gamma^2}, \quad \text{at} \quad y^* = \pm 1. \tag{3.11c}$$

The effective longitudinal dispersivity at $O(Pe_s)$ vanishes

$$D_1^{eff*} = -\frac{1}{2\gamma^2}\int_{-1}^{1} \mathrm{d}y^* \int_{\mathbb{S}} (u^* b_1^* + q_x b_0^*)\mathrm{d}\boldsymbol{q} = 0. \tag{3.12}$$

3.3. *Second order*

At $O(Pe_s^2)$, the average field is governed by

$$\frac{\partial g_2}{\partial t^*} + \frac{\partial}{\partial y^*}\left(q_y g_1 - \gamma^2\frac{\partial g_2}{\partial y^*}\right) + \frac{\partial}{\partial \phi}\left(\Omega_f^* g_2 - \frac{\partial g_2}{\partial \phi}\right) = 0, \tag{3.13a}$$

$$\gamma^2\frac{\partial g_2}{\partial y^*} = q_y g_1 \quad \text{at} \quad y^* = \pm 1, \tag{3.13b}$$

$$\int_{-1}^{1} \mathrm{d}y^* \int_{\mathbb{S}} g_2 \mathrm{d}\boldsymbol{q} = 0. \tag{3.13c}$$

We propose a solution of the form

$$g_2 = K_1(y^*, t^*) + C_1(y^*, t^*)\cos 2\phi + D_1(y^*, t^*)\sin 2\phi. \tag{3.14}$$

The displacement filed at $O(Pe_s^2)$ is governed by

$$\frac{\partial b_2^*}{\partial t^*} + \frac{\partial}{\partial y^*}\left(q_y b_1^* - \gamma^2\frac{\partial b_2^*}{\partial y^*}\right) + \frac{\partial}{\partial \phi}\left(\Omega_f^* b_2^* - \frac{\partial b_2^*}{\partial \phi}\right) = \left(U_0^{eff*} - u^*\right)g_2 + \left(U_1^{eff*} - q_x\right)g_1 + U_2^{eff*} g_0, \tag{3.15a}$$

$$\gamma^2\frac{\partial b_2^*}{\partial y^*} = q_y b_1^* \quad \text{at} \quad y^* = \pm 1, \tag{3.15b}$$

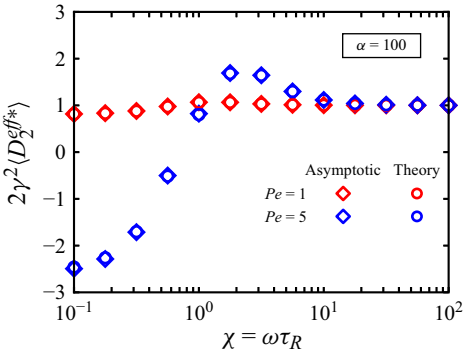

Figure 2. The $O(Pe_s^2)$ dispersivity as a function of χ. For all results, $\alpha = 100$ and $\gamma^2 = 0.1$. Circles denote results obtained from the numerical solutions of the full GTD theory for $Pe_s = 0.1$. Diamonds denote results from the asymptotic analysis.

$$\int_{-1}^{1} \mathrm{d}y^* \int_{\mathbb{S}} b_2^* \mathrm{d}\boldsymbol{q} = 0. \tag{3.15c}$$

We assume a solution for b_2^*

$$b_2^* = K_2(y^*, t^*) + C_2(y^*, t^*)\cos 2\phi + D_2(y^*, t^*)\sin 2\phi. \tag{3.16}$$

One can show that $\langle U_2^{eff*}\rangle = 0$, and

$$D_2^{eff*} = -\frac{1}{2\gamma^2}\int_{-1}^{1} \mathrm{d}y^* \int_{\mathbb{S}} (u^* b_2^* + q_x b_1^*)\mathrm{d}\boldsymbol{q} = -\frac{\pi}{2\gamma^2}\int_{-1}^{1} \left(2u^* K_2 + A_2\right)\mathrm{d}y^*. \tag{3.17}$$

To obtain D_2^{eff*}, one needs to solve for K_2. The relevant equations are given by

$$\frac{\partial K_1}{\partial t^*} - \gamma^2 \frac{\partial^2 K_1}{\partial y^{*2}} + \frac{1}{2}\frac{\partial B_1}{\partial y^*} = 0, \tag{3.18a}$$

$$\frac{\partial K_2}{\partial t^*} + \left[\frac{1}{2}\frac{\partial B_2}{\partial y^*} - \gamma^2 \frac{\partial^2 K_2}{\partial y^{*2}}\right] = U_2^{eff*} g_0 - \frac{1}{2}A_1 + \left(U_0^{eff*} - u^*\right)K_1, \tag{3.18b}$$

$$\frac{\partial K_1}{\partial y^*} = \frac{1}{2\gamma^2}B_1, \quad \text{and} \quad \frac{\partial K_2}{\partial y^*} = \frac{1}{2\gamma^2}B_2 \quad \text{at} \quad y^* = \pm 1. \tag{3.18c}$$

We solve (3.9), (3.11) and (3.18) using a Chebyshev collocation method. For time evolution, we use the Crank–Nicolson method. At long times, the time-averaged dispersion coefficient, $\langle D_2^{eff*}\rangle$, is obtained via numerical integration over one oscillation period. We also solve the full GTD theory by solving (2.27) and (2.30) numerically (see Appendix D). To extract an approximation of D_2^{eff*} from the full solution, denoted as $\tilde{D}_2^{eff*}$, we use the relation $\langle \tilde{D}_2^{eff*}\rangle = (\langle D^{eff*}\rangle - \langle D_0^{eff*}\rangle)/Pe_s^2$. Here, $\langle D_0^{eff*}\rangle$ is the analytical solution for passive particles from (3.6), and the full simulation is performed with $Pe_s = 0.1$.

In figure 2, we plot $\langle D_2^{eff*}\rangle$ as a function of χ. The asymptotic results (diamonds) are compared with numerical solutions (circles) of the full GTD theory (see Appendix D). As in the passive case (see figure 1), the shear-induced dispersion vanishes in the high-frequency limit. From (2.33), we have $\langle D_2^{eff*}\rangle \to 1/(2\gamma^2)$ as $\chi \to \infty$. Indeed, figure 2 shows that $2\gamma^2\langle D_2^{eff*}\rangle$ approaches unity in the high-frequency limit.

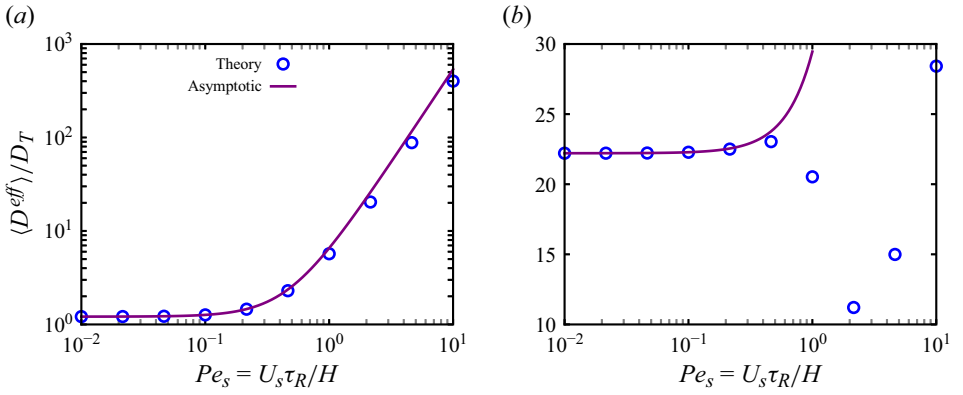

Figure 3. Plots of $\langle D^{eff}\rangle/D_T$ as a function of Pe_s for (*a*) $Pe = 1$ and (*b*) $Pe = 10$. The solid lines denote the two-term asymptotic solution, $\langle D_0^{eff*}\rangle + Pe_s^2\langle D_2^{eff*}\rangle$. Circles are numerical solutions of the full GTD theory. For all results shown, $\chi = 1$, $\gamma^2 = 0.1$ and $\kappa = 0.1$.

Overall, $\langle D_2^{eff*}\rangle$ can be either positive or negative depending on Pe and χ. This means that activity can either enhance or hinder the longitudinal dispersion in an oscillatory flow compared with the passive case. In particular, a reduction in the dispersion ($\langle D_2^{eff*}\rangle < 0$) occurs in the low-frequency regime when Pe is sufficiently large (e.g. $Pe = 5$; blue markers). This reduction can be attributed to shear-reduced swim diffusion (Peng & Brady 2020), which becomes prominent for sufficiently strong shear. For $Pe = 1$, $\langle D_2^{eff*}\rangle > 0$ for all values of χ. For $Pe = 5$, $\langle D_2^{eff*}\rangle$ can be either positive or negative depending on χ. There exists an optimal frequency at which the enhancement in dispersion is maximised.

To understand this effect in association with shear-reduced swim diffusion, recall that the effective dispersion coefficient given by (2.16) consists of three contributions: translational diffusion D_T, shear-modified swim diffusion $-U_s\overline{\tilde{m}_x}$ and classical Taylor dispersion $-\overline{u\tilde{n}}$. The latter two contributions are coupled and therefore should not be interpreted independently as diffusivities. As Pe increases, the fluid vorticity increases proportionally, reducing the effective run length of active particles and thereby suppressing the swim diffusion contribution. In contrast, the Taylor dispersion term increases and becomes significant at larger Pe. As a result, only in the intermediate-Pe regime is the net dispersion reduced compared with the case without flow.

In figure 3, we compare $\langle D^{eff}\rangle/D_T$ from the two-term asymptotic solution (solid lines), $\langle D_0^{eff*}\rangle + Pe_s^2\langle D_2^{eff*}\rangle$, with the numerical solutions (circles) of the full GTD theory. In figure 3(*a*), for $Pe = 1$, the two-term asymptotic solution (solid line) agrees with the full GTD theory (circles) well beyond its formal regime of validity, i.e. $Pe_s \ll 1$. In figure 3(*b*), for a stronger flow ($Pe = 10$), the full GTD results (circles) show that $\langle D^{eff}\rangle/D_T$ varies non-monotonically with increasing Pe_s. As Pe_s increases beyond the weak-swimming regime, the effective dispersivity decreases due to shear-reduced swim diffusion. The effective dispersivity increases again when activity (Pe_s) is sufficiently high. This behaviour is not captured by the asymptotic solution (solid line), which is valid only in the weak-swimming limit.

The above weak-swimming analysis applies to microorganisms in wide channels with moderate run lengths. For *E. coli*, $U_s \sim 30\,\mu\mathrm{m\,s^{-1}}$ (Turner, Ryu & Berg 2000), $\tau_R \sim 1$ s. In a channel of half-width $H \sim 100\,\mu$m, this gives $Pe_s \sim 0.3$. For active particles that

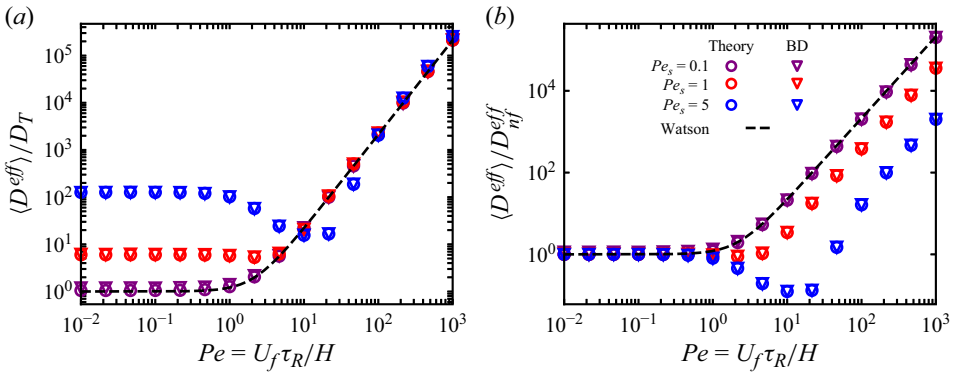

Figure 4. (*a*) Plots of $\langle D^{eff}\rangle/D_T$ as a function of Pe for several values of Pe_s. (*b*) Plots of $\langle D^{eff}\rangle/D_{nf}^{eff}$ as a function of Pe for several values of Pe_s. Circles represent solutions of the full GTD theory, and triangles denote results from BD simulations. The dashed line represents the passive ($Pe_s = 0$) results. For all results, $\chi = 1$, $\gamma^2 = 0.1$ and $\kappa = 0.1$.

have larger run lengths, or in narrower channels, it is then necessary to consider the finite activity regime.

4. Dispersivity in the finite activity regime

To characterise the general behaviour of the effective dispersion coefficient, we resort to numerical solutions of the full GTD theory (see Appendix D). The GTD equations are evolved over time. Numerical solutions of the GTD theory are compared with results obtained from BD simulations (see Appendix C).

4.1. *Competition between flow advection and particle activity*

In this section, we examine the dispersion behaviour of ABPs for a given flow oscillation frequency, $\chi = 1$. With this fixed frequency, the dispersion is qualitatively similar to that considered by Peng & Brady (2020) for a steady Poiseuille flow. In figure 4(*a*), we plot $\langle D^{eff}\rangle/D_T$ as a function of Pe for different values of Pe_s. As $Pe \to 0$, we recover the dispersion coefficient in the absence of flow, D_{nf}^{eff}. Since $D_{nf}^{eff}/D_T = 1 + Pe_s^2/(2\gamma^2)$, the low-$Pe$ plateau in the dispersion coefficient increases with activity (Pe_s). On the other hand, as $Pe \to \infty$, the flow speed dominates over the swim speed. In this regime, the effective dispersion coefficient converges to the passive result (dashed line), regardless of activity. For higher activity (e.g. $Pe_s = 5$; blue markers), a large flow amplitude (Pe) is required for the dispersion coefficient to approach the passive result. For $Pe_s = 0.1$ (purple markers) and $Pe_s = 1$ (red markers), the swimming effects are largely dominated by the Taylor dispersion component. When activity is sufficiently high (e.g. $Pe_s = 5$; blue markers), the dispersion coefficient varies non-monotonically with increasing flow amplitude. The reduction in $\langle D^{eff}\rangle$ for intermediate flow amplitudes is due to the shear-reduced swim diffusion (see also § 3.3).

In figure 4(*b*), we replot the data shown in figure 4(*a*) using a different scaling – $\langle D^{eff}\rangle/D_{nf}^{eff}$ instead of $\langle D^{eff}\rangle/D_T$. By scaling the effective dispersion with the no-flow dispersion coefficient, all curves collapse in the low-Pe limit. Conversely, the rescaled dispersion coefficient approaches different values in the large-Pe limit.

To visualise the non-monotonic behaviour of $\langle D^{eff}\rangle/D_T$, we plot its two contributions, $\langle -U_s\overline{\tilde{m}_x}\rangle/D_T$ and $\langle -\overline{u\tilde{n}}\rangle/D_T$, as functions of Pe in figure 5. In the intermediate Pe

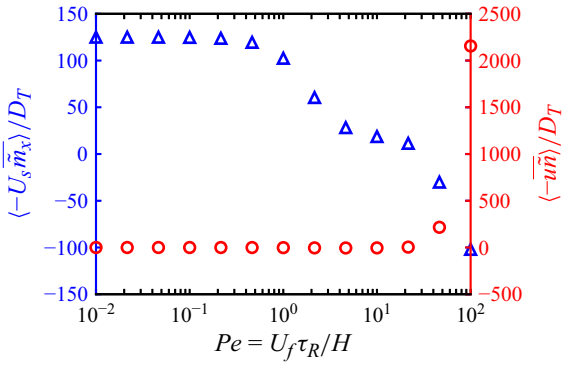

Figure 5. Plots of the two contributions to $\langle D^{eff}\rangle/D_T$, $\langle -U_s\overline{\tilde{m}_x}\rangle/D_T$ and $\langle -\overline{u\tilde{n}}\rangle/D_T$ as a function of Pe for $Pe_s = 5$. Blue triangles represent $\langle -U_s\overline{\tilde{m}_x}\rangle/D_T$, and red circles represent $\langle -\overline{u\tilde{n}}\rangle/D_T$. All results are obtained by solving the full GTD theory with $\chi = 1$, $\gamma^2 = 0.1$ and $\kappa = 0.1$.

regime, $\langle -U_s\overline{\tilde{m}_x}\rangle/D_T$ decreases with increasing Pe and even becomes negative at high Pe. In contrast, $\langle -\overline{u\tilde{n}}\rangle/D_T$ increases with Pe. For sufficiently large Pe, the Taylor component dominates over the swim contribution. The competition between these two contributions gives rise to the observed non-monotonicity in the effective dispersivity, as shown in figure 4. We emphasise that these two contributions are not independent; therefore, each individual term should not be interpreted as a dispersion coefficient.

4.2. *Effect of oscillation frequency*

We now consider the effect of flow oscillation frequency on the effective longitudinal dispersion. In figure 6, we plot $\langle D^{eff}\rangle/D_T$ and $\langle D^{eff}\rangle/D_{nf}^{eff}$ as functions of χ for different values of Pe and Pe_s. Circles denote numerical solutions of the GTD theory, while triangles represent results from BD simulations. The dashed line corresponds to the passive case (i.e. $Pe_s = 0$), as determined by Watson (1983). Figures 6(*a*) and 6(*b*) correspond to $Pe = 10$, whereas figures 6(*c*) and 6(*d*) correspond to $Pe = 40$. To isolate the effect of the oscillation frequency, we fix α in this section. With α fixed, we note that κ depends explicitly on χ (i.e. $\kappa^2 = \chi/\alpha$).

In the high-frequency limit, one can show that the flow vanishes at leading order (see Appendix B for the asymptotic analysis). Effectively, the dispersion in the high-frequency limit is equivalent to the no-flow case. Therefore, $\langle D^{eff}\rangle \to D_{nf}^{eff}$ as $\chi \to \infty$, regardless of Pe_s or Pe. Recall that, in the absence of flow, $\langle D^{eff}\rangle = D_T + D^{swim} = D_T + U_s^2\tau_R/2$, or equivalently $\langle D^{eff}\rangle/D_T = 1 + Pe_s^2/(2\gamma^2)$. As shown in figures 6(*a*) and 6(*c*), in this large-χ limit this leads to larger values of $\langle D^{eff}\rangle/D_T$ for increasing Pe_s. Upon scaling the effective dispersion by D_{nf}^{eff}, the ratio $\langle D^{eff}\rangle/D_{nf}^{eff}$ approaches unity in the high-frequency regime, as shown in figures 6(*b*) and 6(*d*). Compared with the cases shown in figures 6(*a*) and 6(*b*), a higher value of χ is required to reach the high-frequency limit in figures 6(*c*) and 6(*d*), owing to their larger flow amplitudes (Pe). In figures 6(*a*) and 6(*c*), in the low-frequency regime, $\langle D^{eff}\rangle/D_T$ is lower for higher Pe_s, due to the non-monotonic dependence of dispersion on Pe, as discussed in figure 4(*a*) (see also Peng & Brady 2020). For $Pe = 10$ and 40, this regime lies in the range where shear suppresses swim diffusion, while classical Taylor dispersion has not yet become dominant. Consequently, particles with higher swim speeds (e.g. $Pe_s = 5$ versus $Pe_s = 1$) loses a larger fraction of their swim diffusivity. We note that D_{nf}^{eff} depends explicitly on Pe_s. In the low-frequency regime, $\langle D^{eff}\rangle/D_{nf}^{eff}$ is even

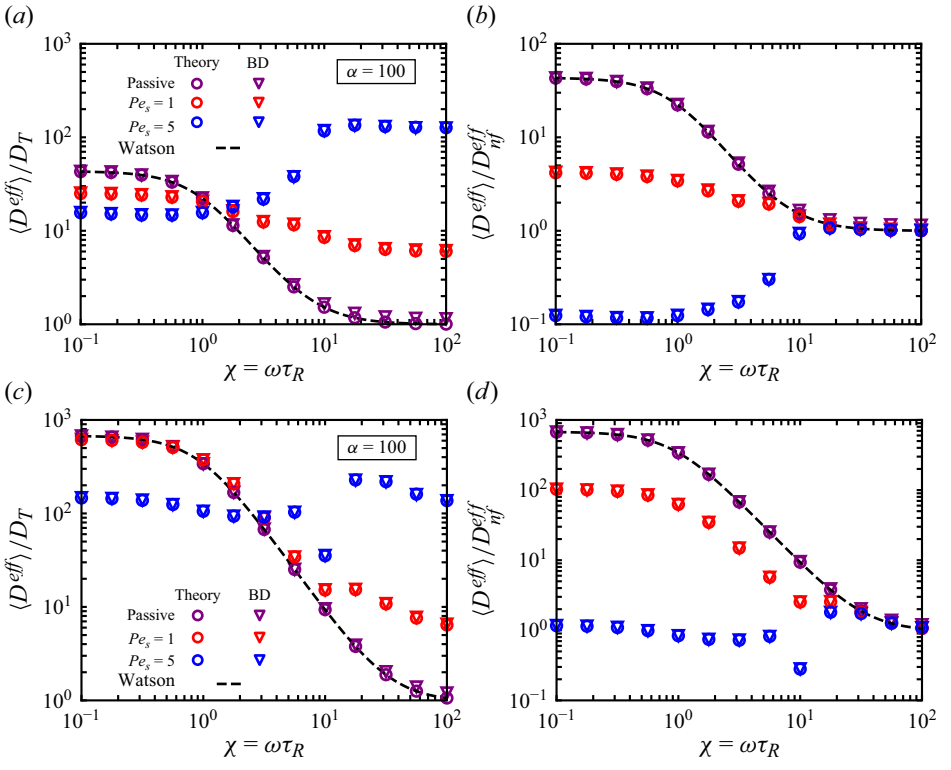

Figure 6. Plots of $\langle D^{eff} \rangle / D_T$ as a function of χ for different values of Pe_s, shown for (*a*) $Pe = 10$ and (*c*) $Pe = 40$. Plots of $\langle D^{eff} \rangle / D_{nf}^{eff}$ as a function χ for different values of Pe_s, shown for (*b*) $Pe = 10$, and (*d*) $Pe = 40$. For all results shown, $\alpha = 100$ and $\gamma^2 = 0.1$. Circles denote results obtained from numerical solutions of the full GTD theory, and triangles represent results from BD simulations. The dashed line indicates the passive ($Pe_s = 0$) solution of Watson (1983).

lower than $\langle D^{eff} \rangle / D_T$ for higher Pe_s because D_{nf}^{eff} increases quadratically with the swim speed, whereas $\langle D^{eff} \rangle$ does not increase as rapidly (see figure 4).

As shown in figure 6, the scaled dispersion coefficient $\langle D^{eff} \rangle / D_{nf}^{eff}$ for passive particles decreases monotonically with χ. For active particles, the scaled dispersion coefficient exhibits a rich behaviour that depends on the flow (Pe) and swim (Pe_s) speeds. At low activity (e.g. $Pe_s = 1$ in figure 6*b*), the scaled dispersion coefficient remains a monotonically decreasing function of χ. For higher activity (e.g. $Pe_s = 5$ in figure 6*b*), the scaled dispersion coefficient begins at a low plateau and increases as a function of χ, eventually converging to the common high-frequency limit.

In figures 6(*c*) and 6(*d*), at low activity ($Pe_s = 1$; red markers), the effective dispersion coefficient $\langle D^{eff} \rangle / D_T$ and the scaled dispersion coefficient $\langle D^{eff} \rangle / D_{nf}^{eff}$ decrease monotonically with χ, exhibiting a plateau around $\chi \sim 10$ and then continue to decrease towards the no-flow limit. However, in figure 6(*d*), the scaled dispersion coefficient exhibits oscillatory behaviour as a function of χ for $Pe_s = 5$. This non-trivial variation occurs when the flow Péclet number is sufficiently large. For $Pe_s = 5$ and $Pe = 40$, we see that $\langle D^{eff} \rangle / D_{nf}^{eff}$ exhibits both a minimum and a maximum at different frequencies. The observed oscillatory behaviour likely results from a resonance in which the flow oscillation time scale matches an intrinsic time scale of the ABPs. Because

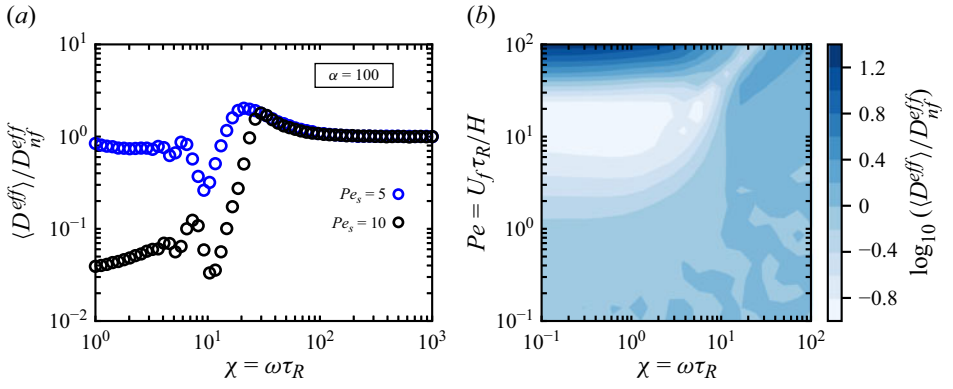

Figure 7. (*a*) Plots of $\langle D^{eff}\rangle/D_{nf}^{eff}$ as a function of χ for different values of Pe_s. (*b*) Contour plot of the logarithm of $\langle D^{eff}\rangle/D_{nf}^{eff}$ as a function of Pe and χ at $Pe_s = 5$. All results are from BD simulations with $\alpha = 100$, and $\gamma^2 = 0.1$. The contour plot is produced from a total of 400 data points, with 20 points uniformly spaced in logarithmic space along each axis.

the dynamics of ABPs involves multiple time scales, the intrinsic time scale that leads to resonant diffusion cannot be easily obtained. In the following, we investigate this phenomenon numerically by identifying the thresholds of this oscillation as a function of χ, Pe and Pe_s. Physically, χ, Pe and Pe_s characterise the flow oscillation time scale $1/\omega$, the flow advection time scale H/U_f and the swimming time scale H/U_s, respectively.

We first examine the details of the oscillation in figure 7(*a*) by plotting $\langle D^{eff}\rangle/D_{nf}^{eff}$ as a function of χ for two values of Pe_s, using more data points than in figure 6. Even though it is not straightforward to determine the intrinsic time scale associated with resonant diffusion, one can rationalise its variation as a function of the swim speed. Compared with $Pe_s = 5$ (blue circles), the onset of oscillatory behaviour of $\langle D^{eff}\rangle/D_{nf}^{eff}$ and the locations of its extrema shift to higher flow frequencies for higher activity ($Pe_s = 10$, black circles). This can be understood by considering the swim time scale, $\tau_s = H/U_s$, which characterises the time it takes for the ABPs to traverse the channel in the transverse direction. As the swim speed (Pe_s) increases, τ_s decreases. Therefore, a smaller flow oscillation time scale (or higher flow oscillation frequency) is required to match the swim time scale.

Next, we consider how the oscillation in the dispersion coefficient further depends on the flow advection. In figure 7(*b*), we show a contour plot of the logarithm of $\langle D^{eff}\rangle/D_{nf}^{eff}$ as a function of Pe and χ for $Pe_s = 5$. We observe that, as Pe increases, the extrema in $\langle D^{eff}\rangle/D_{nf}^{eff}$ shift to higher flow oscillation frequencies, reflected in the upward shift of the light-coloured region in figure 7(*b*) with increasing χ. In addition to the swim time scale discussed in figure 7(*a*), the ABPs in the presence of flow also have a flow time scale defined by H/U_f. As Pe increases, this flow time scale decreases. To achieve resonance, the time scale defined by the flow oscillation, $1/\omega$, needs to be smaller. Due to the interplay of these time scales, in general $\langle D^{eff}\rangle/D_{nf}^{eff}$ exhibits non-monotonic behaviours as a function of Pe and χ. Furthermore, we note that the region where the scaled dispersion coefficient attains low values shrinks as Pe increases.

Together with the behaviour of $\langle D^{eff}\rangle/D_{nf}^{eff}$ shown in figure 7(*a*), we note that increasing either Pe or Pe_s shifts the onset of oscillatory behaviour to higher flow frequencies. This suggests that resonance can occur when the flow oscillation time scale matches some

intrinsic time scale that results from the coupling between the swimming motion and the oscillatory flow advection. Formally, we have $\tau = \tau(Pe_s, Pe)$, where τ is the time scale that must match the flow oscillation time scale to achieve resonance. Extracting the functional dependence of τ on H/U_s and H/U_f is not pursued here. We note that resonant diffusion is commonly observed in both passive and active particle systems (Castiglione *et al.* 1998; Leahy, Koch & Cohen 2015; Chepizhko & Franosch 2022; Khatri & Burada 2022).

4.3. *Non-spherical particles*

We now analyse how the effective dispersivity is influenced by the shape of the particle. For an ellipsoidal particle, a shape factor is defined as $B = (r^2 - 1)/(r^2 + 1)$, where $r = a/b$. Here, a and b denote the lengths of the semi-major and semi-minor axes, respectively. For a sphere, $r = 1$ and $B = 0$. For a thin rod, we have $B \to 1$ as $r \to \infty$. Modelling the angular dynamics using Jeffery equation (Jeffery 1922), we have $\boldsymbol{\Omega}_f = (1/2)\boldsymbol{\nabla} \times \boldsymbol{u}_f + B\boldsymbol{q} \times (\boldsymbol{E} \cdot \boldsymbol{q})$, where $E_{ij} = (1/2)((\partial u_i/\partial x_j) + (\partial u_j/\partial x_i))$ is the rate-of-strain tensor. In the oscillatory Poiseuille flow, we have

$$\Omega'^{*} = \Omega' \tau_D = \frac{(1-i)Pe}{2\kappa}\,(1 - B\cos 2\phi)\,\sinh\left((1+i)\kappa y^{*}\right)\,\mathrm{sech}\,((1+i)\kappa). \tag{4.1}$$

As in the spherical case, we assume a constant translational diffusivity and enforce the no-flux boundary condition (2.4).

In figure 8(*a*), we plot $\langle D^{eff}\rangle/D_T$ as a function Pe for different values of B. The vorticity term ($\boldsymbol{\nabla} \times \boldsymbol{u}_f$) in the angular velocity induces spinning on ABPs, which reduces their persistence and consequently their swim diffusion. For non-spherical particles ($B \neq 0$), the additional alignment term from the rate-of-strain tensor is present. Because of this alignment, non-spherical particles lose less of their persistence. As a result, we observe that in figure 8(*a*), the minimum in the dispersion coefficient decreases as B decreases. As shown in figures 8(*b*) and 8(*c*), the scaled dispersion coefficient $\langle D^{eff}\rangle/D_{nf}^{eff}$ exhibits qualitatively similar behaviour to that of spherical particles. However, the suppression in effective dispersivity is reduced, owing to the reduced spinning.

In the current model, we have assumed an isotropic translational diffusivity for non-spherical particles and applied the same no-flux boundary conditions as for spherical particles (Ezhilan & Saintillan 2015). The anisotropic translational diffusivity of a spheroidal particle can be incorporated into the GTD framework (Kumar *et al.* 2021; Khair 2022). Additional dynamics, such as alignment of a non-spherical particle with the channel wall, may also be included; such effects are expected to modify the dispersion behaviour of non-spherical particles more significantly.

4.4. *Effect of* α

In the results presented so far, we have fixed $\alpha = 100$. We now examine the variation of the effective dispersion coefficient with decreasing α for spherical particles. For a fixed χ and channel geometry, the viscous length $1/\lambda = H\sqrt{\alpha/\chi}$ becomes smaller as α decreases. Consequentially, the flow strength is reduced as α decreases. To visualise the effect of the viscous length on the flow, in figure 9 we plot the norm of u'^{*} (see (2.31)), as a function of y^{*} for different values of α. As shown in figure 9, for a given χ, the amplitude of the flow decreases as α is reduced.

In figure 10, we plot $\langle D^{eff}\rangle/D_{nf}^{eff}$ as a function of χ for different Pe_s and α. For passive particles, $D_{nf}^{eff} = D_T$ and $\langle D^{eff}\rangle = \langle D_0^{eff}\rangle$, where the subscript 0 denotes $Pe_s = 0$ (see § 3). The passive results of Watson (1983) are plotted in figure 10(*a*). Because the flow magnitude is weaker for smaller α, the dispersion coefficient is reduced and

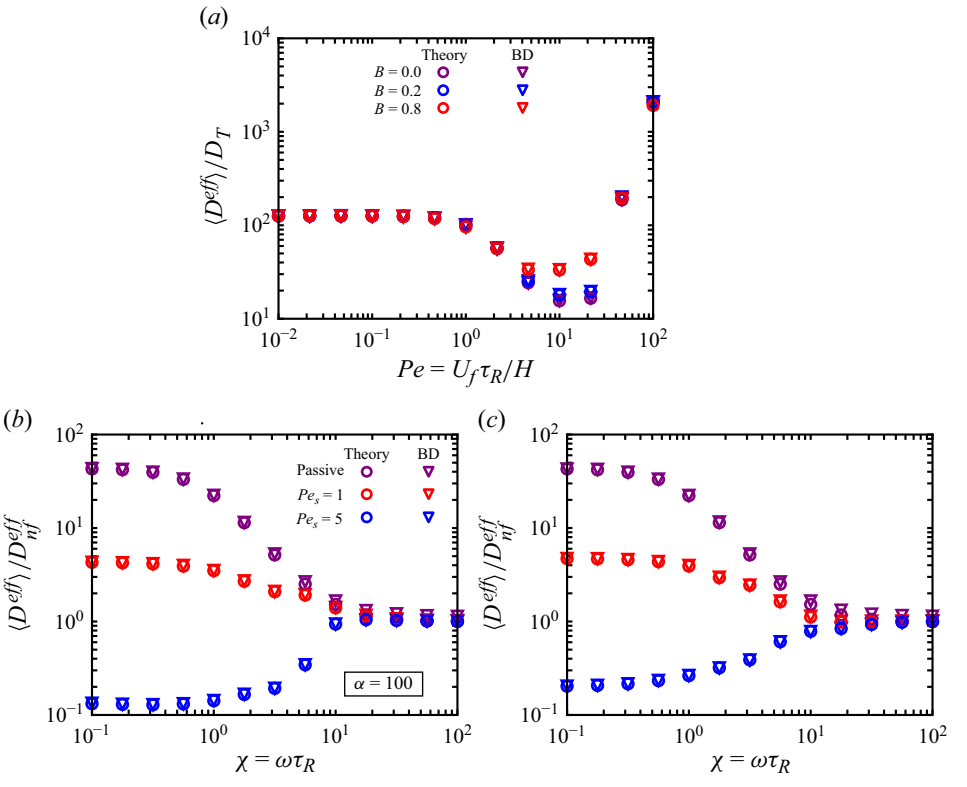

Figure 8. (*a*) Plots of $\langle D^{eff}\rangle/D_T$ as a function of Pe for different values of B. For all results in (*a*), $Pe_s = 5$, $\chi = 1$, $\gamma^2 = 0.1$ and $\kappa = 0.1$. (*b*) Plots of $\langle D^{eff}\rangle/D_{nf}^{eff}$ as a function of χ for $B = 0.2$. (*c*) Plots of $\langle D^{eff}\rangle/D_{nf}^{eff}$ as a function of χ for $B = 0.8$. For all results shown, circles represent results from numerical solutions of the full GTD theory, while triangles denote results from BD simulations. The labels shown in (*b*) also apply to the corresponding curves in (*c*). For (*b*) and (*c*), $Pe = 10$, $\alpha = 100$ and $\gamma^2 = 0.1$.

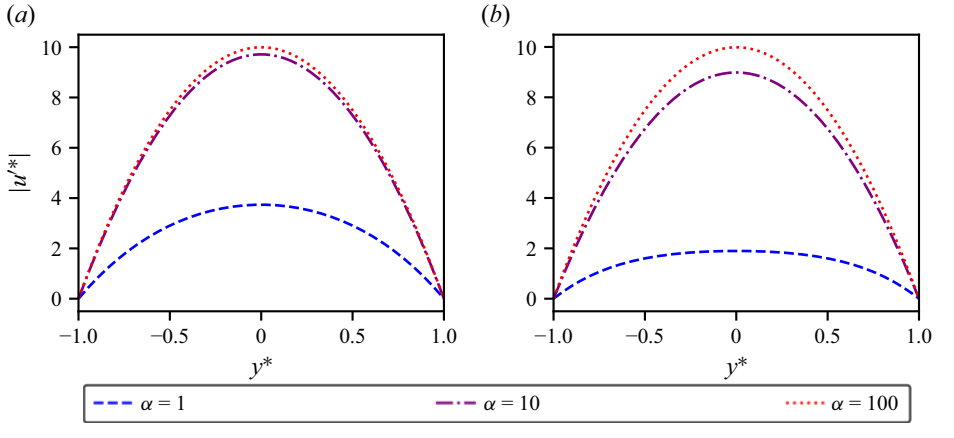

Figure 9. (*a*) Plots of the norm of u'^* as a function of y^* for $\chi = 3$. (*b*) Plots of the norm of u'^* as a function of y^* for $\chi = 6$. For all results shown, $Pe = 10$.

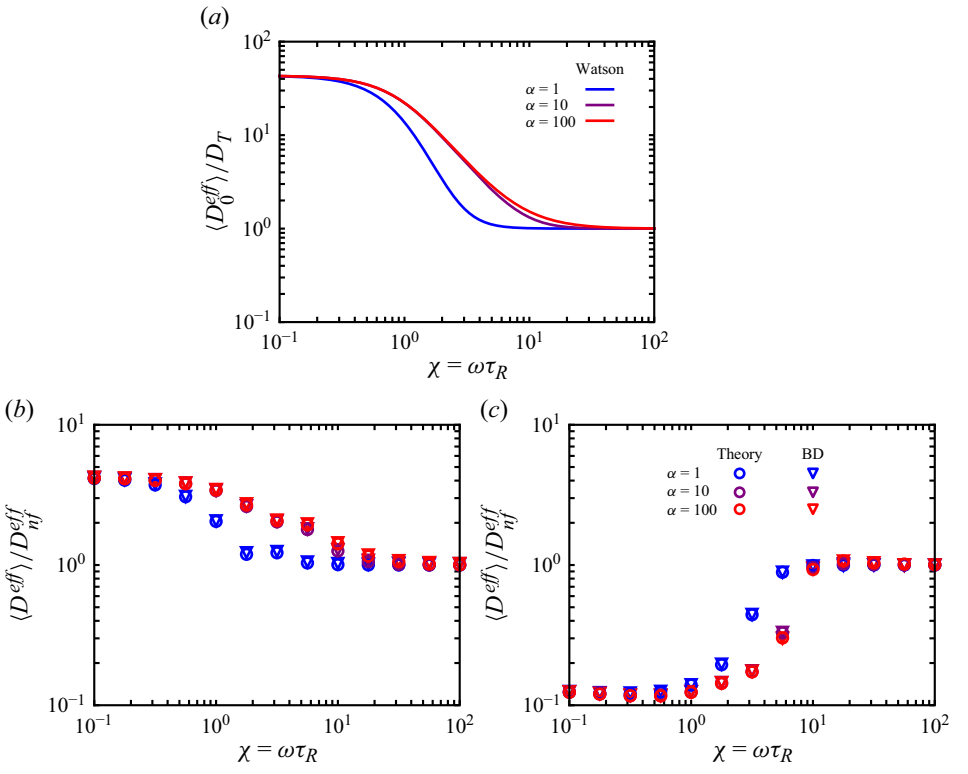

Figure 10. (*a*) Plots of $\langle D^{eff}\rangle/D_{nf}^{eff}$ as a function of χ for different values of α for passive ($Pe_s = 0$) particles. In the absence of activity, $\langle D^{eff}\rangle/D_{nf}^{eff} = \langle D_0^{eff}\rangle/D_T$. (*b*) Plots of $\langle D^{eff}\rangle/D_{nf}^{eff}$ as a function of χ for different values of α for $Pe_s = 1$. (*c*) Plots of $\langle D^{eff}\rangle/D_{nf}^{eff}$ as a function of χ for different values of α for $Pe_s = 5$. For all results shown in (*b*) and (*c*), circles represent results from numerical solutions of the full GTD theory, while triangles denote results from BD simulations. For all results shown, $Pe = 10$ and $\gamma^2 = 0.1$.

approaches its high-frequency limit more rapidly. For weak activity, the same trend as in the passive case is observed ($Pe_s = 1$; see figure 10*b*). At higher activity, the swim diffusivity becomes noticeable. For $Pe_s = 5$ (see figure 10*c*), $\langle D^{eff}\rangle/D_{nf}^{eff}$ is larger for smaller α in the intermediate-χ regime. Regardless of activity, $\langle D^{eff}\rangle/D_{nf}^{eff}$ approaches the high-frequency limit faster for lower α. Because the high-frequency limit exceeds the low-frequency limit in figure 10(*c*), $\langle D^{eff}\rangle/D_{nf}^{eff}$ increases more rapidly for smaller α. By contrast, in figures 10(*a*) and 10(*b*), the high-frequency limits lie below the corresponding low-frequency limits, so decreasing α instead causes $\langle D^{eff}\rangle/D_{nf}^{eff}$ to decrease more rapidly.

5. Concluding remarks

In this paper, we employed a GTD theory to study the longitudinal dispersion of ABPs in oscillatory Poiseuille flow. For passive particles, the time-averaged dispersion coefficient decreases monotonically with increasing flow oscillation frequency. As the frequency increases, Taylor dispersion is gradually suppressed due to the increasing oscillations of the flow. The long-time dispersion can be modelled as a random walk, from which

a diffusivity is defined as ℓ_{eff}^2/τ_{eff}, where ℓ_{eff} is the step length and τ_{eff} is the de-correlation time. In the high-frequency limit, the step length ℓ_{eff} vanishes as a result of the rapid back-and-forth motion induced by the flow. Therefore, Taylor dispersion vanishes and $\langle D^{eff}\rangle \to D_{nf}^{eff} = D_T$ as $\chi \to \infty$. For active particles, we have shown that the high-frequency behaviour is indistinguishable from that of passive particles when the scaled dispersion coefficient $\langle D^{eff}\rangle / D_{nf}^{eff}$ is considered. We note that for active particles $D_{nf}^{eff} = D_T + D^{swim} > D_T$.

We have shown that the effective dispersion coefficient of active particles can exhibit oscillatory behaviour as a function of the flow frequency χ. When the external driving frequency (i.e. flow oscillation frequency) matches an intrinsic frequency, resonant diffusion can be observed. This distinct behaviour of active particles results from the coupling between self-propulsion and oscillatory fluid advection. Without activity, resonant diffusion does not occur. Likewise, for active particles in a steady Poiseuille flow, no oscillatory dispersion arises due to the absence of a periodic driving force. In oscillatory Poiseuille flow, the oscillation frequency acts as an external control parameter that modulates particle dispersion. This modulation is particularly versatile for active particles, as flow oscillations can either enhance or suppress dispersion compared with the no-flow case.

In general, a resonant or oscillatory dynamics may occur when multiple transport mechanisms are present. For example, the rotational dispersion coefficient of axisymmetric Brownian particles in oscillatory shear flows exhibits oscillatory behaviour as a function of the flow frequency (Leahy *et al.* 2015). In this case, the natural frequency corresponds to the inverse of half a Jeffery orbit period, while the external frequency is the flow oscillation frequency. Resonant diffusion has also been observed in particle systems, including the diffusion of chiral particles in steady Poiseuille flow (Khatri & Burada 2022), gravitactic circle swimmers (Chepizhko & Franosch 2022) and particles in complex time-periodic flow fields with mean flow (Castiglione *et al.* 1998).

As is typical in Taylor dispersion theory, we have treated the active particles as point particles, neglecting hydrodynamic interactions with the channel walls. We note that, for active particles, their run length ℓ is often more relevant than the particle size a, particularly when $\ell \gg a$. When the particle size becomes comparable to the channel width, hydrodynamic interactions can no longer be ignored. Wall-induced hydrodynamic effects may qualitatively alter the effective dispersion. Moreover, active particles generate disturbance flows due to their intrinsic force dipoles (Saintillan & Shelley 2014), which can influence both their own motion and that of nearby particles, in contrast to passive particles that only impose no-slip boundary conditions on the surrounding fluid. Incorporating such effects are an important extension of the current model and would be relevant for studying strongly confined swimmers or dense suspensions in microfluidic channels.

In our model, we have assumed that the active particles undergo both translational and rotational Brownian motion. An interesting limit case arises when translational diffusion is absent ($D_T \equiv 0$), such that the active particles are only subject to rotational noise. If D_T is set to zero from the outset, the no-flux boundary conditions (see (2.20) and (2.22)) can no longer be satisfied. To resolve this difficulty, it is necessary to retain D_T in the governing equations and consider a singular perturbation analysis in the limit $D_T \to 0$ (Peng & Brady 2020). In non-dimensional quantities, one can consider the limit $\gamma \to 0$ (see § 2.4). Briefly, diffusive boundary layers will form at both walls, where the diffusive flux balances the swimming flux in order to satisfy the no-flux condition. Alternatively, BD simulations can be used to characterise the dispersion dynamics in the case of zero D_T.

In BD, translational diffusivity can be set directly to zero without introducing any difficulty. For steady Poiseuille flows, active particles without translational Brownian motion are shown to exhibit giant Taylor dispersion, where $D^{eff}/(U_s^2\tau_R/2) \sim Pe^4$ in the strong flow limit (Peng & Brady 2020). From this, we expect that the dispersion of active particles in oscillatory Poiseuille flow without translational noise to exhibit qualitatively different behaviour compared with the case of finite D_T.

While the GTD theory applies to generic time-periodic flows, we have considered only the case where the driving pressure gradient consists of a single harmonic. An interesting extension would be to include a mean flow, in addition to the oscillatory component that averages to zero. Particle transport due to the interaction between the steady and oscillatory components of the flow may lead to qualitatively different dispersion behaviour. In particular, it would be interesting to examine how the oscillatory dispersion behaviour is modified. Furthermore, future work should also explore the dynamics of active particles in generic oscillatory flows composed of multiple harmonics, as coupling between different oscillation modes may give rise to a qualitatively new dispersion dynamics. While our analysis focuses on flows in planar channels, the GTD theory can be generalised to corrugated channels and periodic porous media (Alonso-Matilla *et al.* 2019; Peng 2024). For example, it would be interesting to examine the transport behaviour of active particles in peristaltic flow (Chakrabarti & Saintillan 2020).

Finally, we note that the present analysis has focused on the long-time, asymptotic dispersion characterised by GTD theory. At short times, however, particle transport is governed by pre-asymptotic or transient dispersion, during which the effective longitudinal spreading can differ from its long-time behaviour, and retain memory of the initial conditions and the oscillatory forcing. Transient dispersion has been examined previously for passive and active particles (Mukherjee & Mazumder 1988; Salles *et al.* 1993; Phillips & Kaye 1997; Bandyopadhyay & Mazumder 1999; Vedel & Bruus 2012; Jiang & Chen 2021; Wang *et al.* 2022; Guan *et al.* 2023; Zeng *et al.* 2024). An important direction for future work is to consider the transient dispersion of active particles in oscillatory flows.

Acknowledgements. The authors acknowledge the Digital Research Alliance of Canada for providing computational resources. Z.P. also acknowledges the Erskine Fellowship at the University of Canterbury, during which part of this work was completed.

Funding. Z.P. was supported by the Discovery Grants program (grant no. RGPIN-2025-05310) of the Natural Sciences and Engineering Research Council of Canada (NSERC).

Declaration of interests. The authors report no conflicts of interest.

Appendix A. The passive solution

The displacement field at $O(1)$ is governed by

$$\frac{\partial b_0^*}{\partial t^*} + \frac{\partial}{\partial y^*}\left(-\gamma^2\frac{\partial b_0^*}{\partial y^*}\right) + \frac{\partial}{\partial \phi}\left(\Omega_f^* b_0^* - \frac{\partial b_0^*}{\partial \phi}\right) = \left(U_0^{eff*} - u^*\right) g_0, \tag{A1a}$$

$$-\frac{\partial b_0^*}{\partial y^*} = 0, \quad \text{at} \quad y^* = \pm 1, \tag{A1b}$$

$$\int_{-1}^{1} \mathrm{d}y^* \int_{\mathbb{S}} b_0^* \mathrm{d}\boldsymbol{q} = 0, \tag{A1c}$$

which admits a solution of the form $b_0^* = \mathrm{Re}[A_0'(y^*)e^{i\chi t^*}/(2\pi)]$. Here, A_0' satisfies

$$i\chi A_0' - \gamma^2 \frac{d^2 A_0'}{dy^{*2}} = \overline{u'^*} - u'^*, \tag{A2a}$$

$$-\frac{dA_0'}{dy^*} = 0, \quad \text{at} \quad y^* = \pm 1, \tag{A2b}$$

$$\int_{-1}^{1} A_0' dy^* = 0. \tag{A2c}$$

One can show that the solution is given by

$$A_0'(y^*) = \alpha_0 + \alpha_1 \cosh\left((1+i)\frac{\sqrt{\chi}}{\sqrt{2}\gamma} y^*\right) + \alpha_2 \cosh\left((1+i)\kappa y^*\right), \tag{A3}$$

where

$$\alpha_0 = \frac{Pe(1-i)}{2\kappa^3 \chi} \tanh\left((1+i)\kappa\right), \tag{A4a}$$

$$\alpha_1 = -\frac{\sqrt{2} Pe\, \gamma}{\chi^{1/2}\kappa\left(2\kappa^2\gamma^2 - \chi\right)} \frac{\tanh\left((1+i)\kappa\right)}{\sinh(1+i)\frac{\sqrt{\chi}}{\sqrt{2}\gamma}}, \tag{A4b}$$

$$\alpha_2 = \frac{Pe}{\kappa^2\left(2\kappa^2\gamma^2 - \chi\right)} \mathrm{sech}\left((1+i)\kappa\right). \tag{A4c}$$

One interesting limit is $\kappa \to 0$, where the viscous length scale, $\sqrt{2\nu/\omega}$, is much larger than the channel half-width, H. As $\kappa \to 0$, we have

$$\alpha_0 = \frac{Pe}{\chi\kappa^2} + O(\kappa^2), \quad \alpha_2 = -\frac{Pe}{\chi\kappa^2} + O(\kappa^2), \tag{A5a}$$

$$\alpha_1 = \frac{(1+i)\sqrt{2}Pe}{\chi^{3/2}} \frac{1}{\sinh\left((1+i)\frac{\sqrt{\chi}}{\sqrt{2}\gamma}\right)} + O(\kappa^2), \tag{A5b}$$

$$\cosh\left((1+i)\kappa y^*\right) = 1 + O(\kappa^2). \tag{A5c}$$

Therefore, the singular contributions from α_0 and $\alpha_2 \cosh[(1+i)\kappa y^*]$ in (A3) are cancelled out while the second term in (A3) is regular. Overall $A_0'(y^*)$ is finite as $\kappa \to 0$

$$A_0'(y^*) = \frac{Pe}{3\chi^2}\left(-6\gamma^2 + i\left(1 - 3y^{*2}\right)\chi\right) + \frac{\sqrt{2}Pe\,\gamma\,(1+i)}{\chi^{3/2}} \frac{\cosh\left((1+i)\frac{\sqrt{\chi}}{\sqrt{2}\gamma} y^*\right)}{\sinh\left((1+i)\frac{\sqrt{\chi}}{\sqrt{2}\gamma}\right)} + O(\kappa^2). \tag{A6}$$

Another limit that we examine is $\chi \to 0$. In this limit, we have

$$\alpha_0 = \left(\frac{1}{2} - \frac{i}{2}\right) \frac{Pe}{\kappa^3\chi} \tanh\left((1+i)\kappa\right) + O(\chi^3), \tag{A7a}$$

$$\alpha_1 = -\left(\frac{1}{2} - \frac{i}{2}\right)\frac{Pe}{\kappa^3\chi}\tanh\left((1+i)\kappa\right) + O(\chi), \tag{A7b}$$

$$\alpha_2 = \frac{Pe}{2\gamma^2\kappa^4}\operatorname{sech}\left((1+i)\kappa\right) + O(\chi), \tag{A7c}$$

$$\cosh\left((1+i)\frac{\sqrt{\chi}}{\sqrt{2}\gamma}y^*\right) = 1 + O(\chi). \tag{A7d}$$

The singular contributions from α_0 and $\alpha_1\cosh\left((1+i)(\sqrt{\chi}/\sqrt{2}\gamma)y^*\right)$ in (A3) are cancelled out while the third term in (A3) is regular. Overall $A_0'(y^*)$ is finite as $\chi \to 0$

$$A_0'(y^*) = \frac{Pe}{2\gamma^2\kappa^4}\frac{\cosh\left((1+i)y^*\kappa\right)}{\cos\left((1+i)\kappa\right)} + \frac{(1+i)Pe}{12\gamma^2\kappa^5}\left[3i + \left(1 - 3y^{*2}\right)\kappa^2\right]\tanh\left((1+i)\kappa\right) + O(\chi). \tag{A8}$$

The last limit that we consider is $(2\kappa^2\gamma^2 - \chi) \to 0$. We define $\epsilon = (2\kappa^2\gamma^2 - \chi)$. This limit $\epsilon \to 0$ is of particular interest when we look at (A4*b*) and (A4*c*). We show that in this limit

$$\alpha_0 = \left(\frac{1}{4} - \frac{i}{4}\right)\frac{Pe}{\gamma^2\kappa^5}\tanh\left((1+i)\kappa\right) + O(\epsilon), \tag{A9a}$$

$$\alpha_1 = -\frac{Pe}{\kappa^2\epsilon}\operatorname{sech}\left((1+i)\kappa\right) + O(\epsilon), \tag{A9b}$$

$$\alpha_2 = \frac{Pe}{\kappa^2\epsilon}\operatorname{sech}\left((1+i)\kappa\right) + O\left(\epsilon^3\right), \tag{A9c}$$

$$\cosh\left((1+i)\frac{\sqrt{\chi}}{\sqrt{2}\gamma}y^*\right) = \cosh\left((1+i)\kappa y^*\right) + O(\epsilon). \tag{A9d}$$

The singular contributions from $\alpha_1\cosh\left((1+i)(\sqrt{\chi}/\sqrt{2}\gamma)y^*\right)$ and $\alpha_2\cosh\left((1+i)\kappa y^*\right)$ are cancelled out while the first term in (A3) is regular. This shows in the limit $\epsilon \to 0$, $A_0'(y^*)$ is finite, and $A_0'(y^*)$ takes the form

$$A_0'(y^*) = \eta_0 + \eta_1\cosh\left((1+i)y^*\kappa\right) + \eta_2\sinh\left((1+i)y^*\kappa\right) + O(\epsilon), \tag{A10}$$

where

$$\eta_0 = \frac{(1-i)Pe}{4\gamma^2\kappa^5}\tanh\left((1+i)\kappa\right) - \frac{Pe}{4\gamma^2\kappa^4}\frac{1}{\sinh\left((1+i)\kappa\right)}, \tag{A11a}$$

$$\eta_1 = 1 + (1+i)\kappa\coth\left((1+i)\kappa\right), \tag{A11b}$$

$$\eta_2 = -y^*(1+i)\kappa\tanh\left((1+i)\kappa\right). \tag{A11c}$$

Appendix B. The high-frequency limit

Here, we analyse the governing (2.27) and (2.30) in the high-frequency limit characterised by $\chi \gg 1$ while keeping the ratio $\chi/\kappa^2 = \alpha = 2\nu\tau_R/H^2$ constant. That is, $\alpha = O(1)$ as $\chi \to \infty$. We also assume that all other non-dimensional parameters are $O(1)$ as $\chi \to \infty$. To facilitate our analysis, we write the long-time solution to g as a Fourier series

$$g(y^*, \phi, t^*) = \sum_{n=-\infty}^{+\infty} e^{in\chi t^*} g_n(y^*, \phi). \tag{B1}$$

Inserting this expansion into (2.27), we obtain

$$in\chi g_n + Pe_s \sin\phi \frac{\partial g_n}{\partial y^*} - \gamma^2 \frac{\partial^2 g_n}{\partial y^{*2}} + \frac{\partial}{\partial \phi}\left[\mathrm{Re}\left(\Omega'^*\right)\frac{1}{2}\left(g_{n-1}+g_{n+1}\right) - \mathrm{Im}\left(\Omega'^*\right)\frac{1}{2i}\left(g_{n-1}-g_{n+1}\right)\right] - \frac{\partial^2 g_n}{\partial \phi^2} = 0. \quad \text{(B2)}$$

The conservation condition becomes

$$\frac{1}{2}\int_{-1}^{1} \mathrm{d}y^* \int_0^{2\pi} \mathrm{d}\phi \sum_{n=-\infty}^{+\infty} e^{in\chi t^*} g_n(y^*, \phi) = 1. \quad \text{(B3)}$$

Making use of orthogonality, we have

$$\frac{1}{2}\int_{-1}^{1} \mathrm{d}y^* \int_0^{2\pi} \mathrm{d}\phi\, g_0(y^*, \phi) = 1, \quad \text{and} \quad \int_{-1}^{1} \mathrm{d}y^* \int_0^{2\pi} \mathrm{d}\phi\, g_n(y^*, \phi) = 0,\ n \neq 0. \quad \text{(B4)}$$

In the high-frequency limit, one can show that $g_0 = O(1)$ and $g_1 = o(1)$. At leading order, we have

$$Pe_s \sin\phi \frac{\partial g_0}{\partial y^*} - \gamma^2 \frac{\partial^2 g_0}{\partial y^{*2}} - \frac{\partial^2 g_0}{\partial \phi^2} = 0. \quad \text{(B5)}$$

The no-flux condition is given by

$$Pe_s \sin\phi\, g_0 - \gamma^2 \frac{\partial g_0}{\partial y^*} = 0, \quad y^* = \pm 1. \quad \text{(B6)}$$

This shows that, at high frequencies, the governing equation for g, to leading order, reduces to that of ABPs in a channel without flow. Similarly, one can show that the displacement field also satisfies the equation without flow. As a result, the effective dispersion coefficient approaches the no-flow result in the high-frequency limit.

Appendix C. Brownian dynamics

The discretised Langevin equations are given by

$$x_{n+1} = x_n + u_f\,(y_n, t_n)\,\Delta t + U_s \cos(\phi_n)\,\Delta t + \Delta x^B, \quad \text{(C1}a\text{)}$$

$$y_{n+1} = y_n + U_s \sin(\phi_n)\,\Delta t + \Delta y^B, \quad \text{(C1}b\text{)}$$

$$\phi_{n+1} = \phi_n + \Omega_f(y_n, \phi_n, t_n)\Delta t + \Delta\phi^B, \quad \text{(C1}c\text{)}$$

where Δt is the time step. The Brownian displacements Δx^B, Δy^B and $\Delta\phi^B$ are sampled from independent white noise processes. The translational Brownian displacement has a variance of $2D_T\Delta t$, and the rotary Brownian displacement has a variance of $2\Delta t/\tau_R$. A potential-free algorithm is used to implement the no-flux condition (Heyes & Melrose 1993). For all simulations, a sufficiently small time step is used to resolve all the physical time scales in the system. The total simulation time is long enough to ensure convergence to the long-time behaviour. A time step in the range $10^{-6}\tau_R$–$10^{-5}\tau_R$ is used. To ensure good statistics, all simulations are performed with 200 000 particles.

In figure 11, we show the transient behaviour of the mean displacement $\langle x - x_0\rangle/H$ as a function of t/τ_R, for different values of χ and for different values of Pe_s. Here, x_0 is the

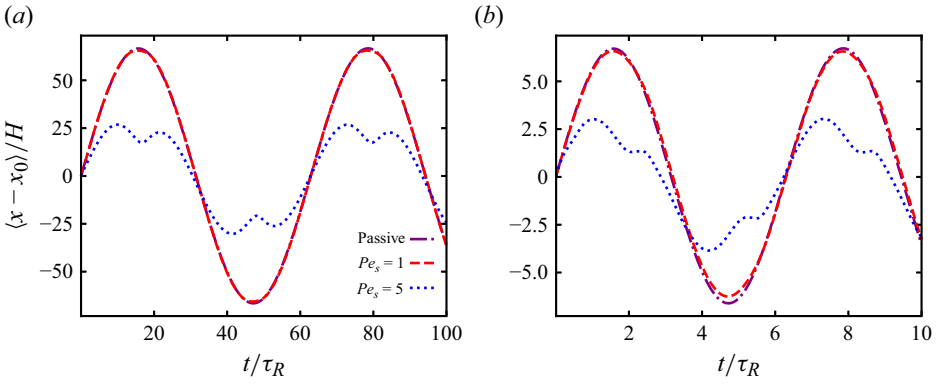

Figure 11. Plots of the mean displacement in the x direction, $\langle x - x_0 \rangle / H$, as a function of t/τ_R for different values of Pe_s for (*a*) $\chi = 0.1$ and (*b*) $\chi = 1$. All results are from BD simulations with $\alpha = 100$, $\gamma^2 = 0.1$ and $Pe = 10$.

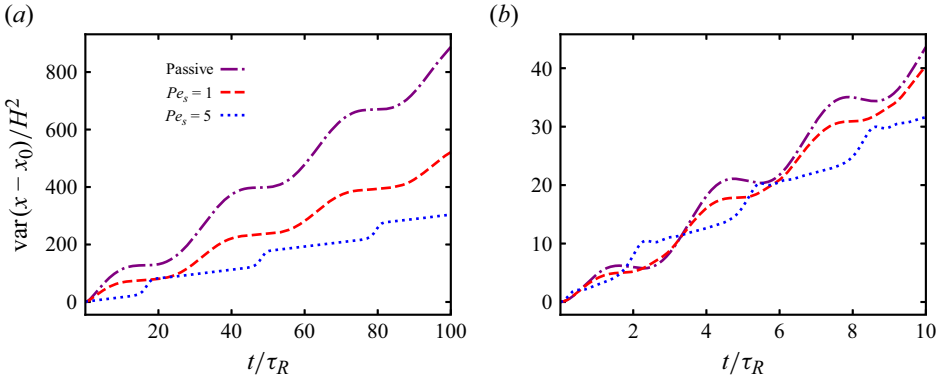

Figure 12. Plots of the variance in the x direction, $\mathrm{var}(x - x_0)/H^2$, as a function of t/τ_R for different values of Pe_s for (*a*) $\chi = 0.1$ and (*b*) $\chi = 1$. All results are from BD simulations with $\alpha = 100$, $\gamma^2 = 0.1$ and $Pe = 10$.

initial x position of particles. At long times, the mean displacement follows the oscillatory behaviour of the flow, as it oscillates around zero. In figure 12, we show the transient behaviour of the variance $\mathrm{var}(x - x_0)/H^2$ as a function of t/τ_R, for different values of χ and for different values of Pe_s. The variance grows with time while exhibiting oscillations that reflect the time-periodic nature of the flow.

Appendix D. Numerical simulation

The governing (2.27) and (2.30) are solved numerically using Dedalus (Burns *et al.* 2020). The physical space (y^*) is discretised on a Chebyshev grid with 128 nodes, and the orientational space is represented in Fourier space with 128 nodes. For time integration, we employ a second-order Crank–Nicolson–Adams–Bashforth scheme. A typical time step of 10^{-6} is used. In the high-frequency regime, the time step is further reduced to 10^{-7}.

References

Alonso-Matilla, R., Chakrabarti, B. & Saintillan, D. 2019 Transport and dispersion of active particles in periodic porous media. *Phys. Rev. Fluids* **4** (4), 043101.

Anand, S.K. & Singh, S.P. 2021 Migration of active filaments under Poiseuille flow in a microcapillary tube. *Eur. Phys. J. E* **44**, 1–10.

Apaza, L. & Sandoval, M. 2016 Ballistic behavior and trapping of self-driven particles in a Poiseuille flow. *Phys. Rev. E* **93** (6), 062602.

Aris, R. 1956 On the dispersion of a solute in a fluid flowing through a tube. *Proc. R. Soc. Lond. A* **235** (1200), 67–77.

Aris, R. 1960 On the dispersion of a solute in pulsating flow through a tube. *Proc. R. Soc. Lond. A* **259** (1298), 370–376.

Bandyopadhyay, S. & Mazumder, B.S. 1999 Unsteady convective diffusion in a pulsatile flow through a channel. *Acta Mechanica* **134** (1), 1–16.

Bechinger, C., Di Leonardo, R., Löwen, H., Reichhardt, C., Volpe, G. & Volpe, G. 2016 Active particles in complex and crowded environments. *Rev. Mod. Phys.* **88** (4), 045006.

Berg, H.C. 1993 *Random Walks in Biology*. Princeton University Press.

Berg, H.C. 2004 *E. Coli in Motion*. Springer.

Berg, H.C. & Brown, D.A. 1972 Chemotaxis in Escherichia coli analysed by three-dimensional tracking. *Nature* **239** (5374), 500–504.

Bowden, K.F. 1965 Horizontal mixing in the sea due to a shearing current. *J. Fluid Mech.* **21** (1), 83–95.

Brenner, H. 1980 Dispersion resulting from flow through spatially periodic porous media. *Phil. Trans. R. Soc. Lond. A Math. Phys. Sci.* **297** (1430), 81–133.

Brenner, H. 2013 *Macrotransport Processes*. Elsevier.

Van den Broeck, C. 1982 A stochastic description of longitudinal dispersion in uniaxial flows. *Phys. A* **112** (1–2), 343–352.

Burns, K.J., Vasil, G.M., Oishi, J.S., Lecoanet, D. & Brown, B.P. 2020 Dedalus: a flexible framework for numerical simulations with spectral methods. *Phys. Rev. Res.* **2** (2), 023068.

Caldag, H.O. & Bees, M.A. 2025 Fine-tuning the dispersion of active suspensions with oscillatory flows. *Phil. Trans. R. Soc. Lond. A* **383**, 2304.

Castiglione, P., Crisanti, A., Mazzino, A., Vergassola, M. & Vulpiani, A. 1998 Resonant enhanced diffusion in time-dependent flow. *J. Phys. A* **31** (35), 7197.

Chakrabarti, B. & Saintillan, D. 2020 Shear-induced dispersion in peristaltic flow. *Phys. Fluids* **32** (11), 113102.

Chakraborty, R., Maiti, A., Sharma, N. & Dey, K.K. 2022 Active matter dynamics in confined microfluidic environments. *Prog. Mol. Biol. Trans. Sci.* **186** (1), 245–265.

Chandragiri, S., Doostmohammadi, A., Yeomans, J.M. & Thampi, S.P. 2020 Flow states and transitions of an active nematic in a three-dimensional channel. *Phys. Rev. Lett.* **125** (14), 148002.

Chatwin, P.C. 1975 On the longitudinal dispersion of passive contaminant in oscillatory flows in tubes. *J. Fluid Mech.* **71** (3), 513–527.

Chatwin, P.C. 1977 The initial development of longitudinal dispersion in straight tubes. *J. Fluid Mech.* **80** (1), 33–48.

Chepizhko, O. & Franosch, T. 2022 Resonant diffusion of a gravitactic circle swimmer. *Phys. Rev. Lett.* **129** (22), 228003.

Choudhary, A., Paul, S., Rühle, F. & Stark, H. 2022 How inertial lift affects the dynamics of a microswimmer in Poiseuille flow. *Commun. Phys.* **5** (1), 14.

Chu, H.C.W., Garoff, S., Przybycien, T.M., Tilton, R.D. & Khair, A.S. 2019 Dispersion in steady and time-oscillatory two-dimensional flows through a parallel-plate channel. *Phys. Fluids* **31** (2), 022007.

Chu, H.C.W., Garoff, S., Tilton, R.D. & Khair, A.S. 2020 Dispersion in steady and time-oscillatory flows through an eccentric annulus. *AIChE J.* **66** (2), e16831.

Chuphal, P., Sahoo, S. & Thakur, S. 2021 Effect of Poiseuille flow on the dynamics of active vesicle. *Soft Mater.* **19** (3), 359–372.

Díez, P., Lucena-Sánchez, E., Escudero, A., Llopis-Lorente, A., Villalonga, R. & Martinez-Manez, R. 2021 Ultrafast directional janus Pt–mesoporous silica nanomotors for smart drug delivery. *ACS Nano* **15** (3), 4467–4480.

Ezhilan, B. & Saintillan, D. 2015 Transport of a dilute active suspension in pressure-driven channel flow. *J. Fluid Mech.* **777**, 482–522.

Figueroa-Morales, N., Rivera, A., Soto, R., Lindner, A., Altshuler, E. & Clément, É. 2020 *E. coli* 'super-contaminates' narrow ducts fostered by broad run-time distribution. *Sci. Adv.* **6** (11), eaay0155.

GANESH, A., DOUARCHE, C., DENTZ, M. & AURADOU, H. 2023 Numerical modeling of dispersion of swimming bacteria in a Poiseuille flow. *Phys. Rev. Fluids* **8** (3), 034501.
GHOSH, A., XU, W., GUPTA, N. & GRACIAS, D. 2020 Active matter therapeutics. *Nano Today* **31**, 100836.
GOMEZ-SOLANO, J.R., BLOKHUIS, A. & BECHINGER, C. 2016 Dynamics of self-propelled janus particles in viscoelastic fluids. *Phys. Rev. Lett.* **116** (13), 138301.
GUAN, M., JIANG, W., WANG, B., ZENG, L., LI, Z. & CHEN, G. 2023 Pre-asymptotic dispersion of active particles through a vertical pipe: the origin of hydrodynamic focusing. *J. Fluid Mech.* **962**, A14.
HETTIARACHCHI, H.D.M., HSU, Y., HARRIS, T.J. & LINNINGER, A.A. 2011 The effect of pulsatile flow on intrathecal drug delivery in the spinal canal. *Ann. Biomed. Engng* **39**, 2592–2602.
HEYES, D.M. & MELROSE, J.R. 1993 Brownian dynamics simulations of model hard-sphere suspensions. *J. Non-Newtonian Fluid Mech.* **46** (1), 1–28.
HILL, N.A. & BEES, M.A. 2002 Taylor dispersion of gyrotactic swimming micro-organisms in a linear flow. *Phys. Fluids* **14** (8), 2598–2605.
JEFFERY, G.B. 1922 The motion of ellipsoidal particles immersed in a viscous fluid. *Proc. R. Soc. Lond. A* **102** (715), 161–179.
JIANG, W. & CHEN, G. 2021 Transient dispersion process of active particles. *J. Fluid Mech.* **927**, A11.
JING, G., ZÖTTL, A., CLÉMENT, É. & LINDNER, A. 2020 Chirality-induced bacterial rheotaxis in bulk shear flows. *Sci. Adv.* **6** (28), eabb2012.
JUNOT, G., FIGUEROA-MORALES, N., DARNIGE, T., LINDNER, A., SOTO, R., AURADOU, H. & CLÉMENT, E. 2019 Swimming bacteria in Poiseuille flow: the quest for active Bretherton–Jeffery trajectories. *Europhys. Lett.* **126** (4), 44003.
KANTSLER, V., DUNKEL, J., BLAYNEY, M. & GOLDSTEIN, R.E. 2014 Rheotaxis facilitates upstream navigation of mammalian sperm cells. *eLife* **3**, e02403.
KAYA, T. & KOSER, H. 2012 Direct upstream motility in Escherichia coli. *Biophys. J.* **102** (7), 1514–1523.
KHAIR, A.S. 2022 Taylor dispersion of elongated rods at small and large rotational Péclet numbers. *Phys. Rev. Fluids* **7** (1), 014502.
KHATRI, N. & BURADA, P.S. 2022 Diffusion of chiral active particles in a Poiseuille flow. *Phys. Rev. E.* **105** (2), 024604.
KIM, M.K., DRESCHER, K., PAK, O.S., BASSLER, B.L. & STONE, H.A. 2014 Filaments in curved streamlines: rapid formation of staphylococcus aureus biofilm streamers. *New J. Phys.* **16** (6), 065024.
KUMAR, A.H., THOMSON, S.J., POWERS, T.R. & HARRIS, D.M. 2021 Taylor dispersion of elongated rods. *Phys. Rev. Fluids* **6** (9), 094501.
LAGOIN, M., LACHEREZ, J., DE TOURNEMIRE, G., BADR, A., AMAROUCHENE, Y., ALLARD, A., SALEZ, T. 2025 Enhanced dispersion of active microswimmers in confined flows. *Proc. Natl Acad. Sci. USA* **122** (50), e2519691122.
LANE, M.C., LOCKATELL, V., MONTEROSSO, G., LAMPHIER, D., WEINERT, J., HEBEL, J.R., JOHNSON, D.E. & MOBLEY, H.L.T. 2005 Role of motility in the colonization of uropathogenic Escherichia coli in the urinary tract. *Infection Immunity* **73** (11), 7644–7656.
LEAHY, B.D., KOCH, D.L. & COHEN, I. 2015 The effect of shear flow on the rotational diffusion of a single axisymmetric particle. *J. Fluid Mech.* **772**, 42–79.
LIN, R., YU, W., CHEN, X. & GAO, H. 2021 Self-propelled micro/nanomotors for tumor targeting delivery and therapy. *Adv. Healthcare Mater.* **10** (1), 2001212.
MATHIJSSEN, A.J.T.M., FIGUEROA-MORALES, N., JUNOT, G., CLÉMENT, É., LINDNER, A. & ZÖTTL, A. 2019 Oscillatory surface rheotaxis of swimming E. coli bacteria. *Nat. Commun.* **10** (1), 3434.
MAZUMDER, B.S. & DAS, S.K. 1992 Effect of boundary reaction on solute dispersion in pulsatile flow through a tube. *J. Fluid Mech.* **239**, 523–549.
MCDONALD, D.A. 1955 The relation of pulsatile pressure to flow in arteries. *J. Physiol.* **127** (3), 533.
MUKHERJEE, A. & MAZUMDER, B.S. 1988 Dispersion of contaminant in oscillatory flows. *Acta Mechanica* **74** (1), 107–122.
NG, C.-O. 2006 Dispersion in steady and oscillatory flows through a tube with reversible and irreversible wall reactions. *Proc. R. Soc. Lond. A* **462** (2066), 481–515.
OMORI, T. & ISHIKAWA, T. 2016 Upward swimming of a sperm cell in shear flow. *Phys. Rev. E.* **93** (3), 032402.
PARK, B.-W., ZHUANG, J., YASA, O. & SITTI, M. 2017 Multifunctional bacteria-driven microswimmers for targeted active drug delivery. *ACS Nano* **11** (9), 8910–8923.
PENG, Z. 2024 Macrotransport of active particles in periodic channels and fields: rectification and dispersion. *J. Chem. Phys.* **161** (15), 154101.
PENG, Z. & BRADY, J.F. 2020 Upstream swimming and Taylor dispersion of active Brownian particles. *Phys. Rev. Fluids* **5** (7), 073102.

PHILLIPS, C.G. & KAYE, S.R. 1997 The initial transient of concentration during the development of Taylor dispersion. *Proc. R. Soc. Lond. A* **453**, 2669–2688, 1967.

PLAN, E.L.C.V.I.M., YEOMANS, J.M. & DOOSTMOHAMMADI, A. 2020 Active matter in a viscoelastic environment. *Phys. Rev. Fluids* **5** (2), 023102.

ROMANCZUK, P., BÄR, M., EBELING, W., LINDNER, B. & SCHIMANSKY-GEIER, L. 2012 Active Brownian particles: from individual to collective stochastic dynamics. *Eur. Phys. J. Special Topics* **202**, 1–162.

RUSCONI, R., LECUYER, S., GUGLIELMINI, L. & STONE, H.A. 2010 Laminar flow around corners triggers the formation of biofilm streamers. *J. R. Soc. Interface* **7** (50), 1293–1299.

SAINTILLAN, D. & SHELLEY, M.J. 2014 Theory of active suspensions. In *Complex Fluids in Biological Systems: Experiment, Theory, and Computation*, pp. 319–355. Springer.

SALLES, J., THOVERT, J.-F., DELANNAY, R., PREVORS, L., AURIAULT, J.-L. & ADLER, P.M. 1993 Taylor dispersion in porous media. Determination of the dispersion tensor. *Phys. Fluids* **5** (10), 2348–2376.

SCHWEITZER, F., EBELING, W. & TILCH, B. 1998 Complex motion of Brownian particles with energy depots. *Phys. Rev. Lett.* **80** (23), 5044.

SECOMB, T.W. 2016 Hemodynamics. *Comprehensive Physiol.* **6** (2), 975.

SHAPIRO, M. & BRENNER, H. 1990 Taylor dispersion in the presence of time-periodic convection phenomena. Part II. Transport of transversely oscillating Brownian particles in a plane Poiseuille flow. *Phys. Fluids A* **2** (10), 1744–1753.

SIITONEN, A. & NURMINEN, M. 1992 Bacterial motility is a colonization factor in experimental urinary tract infection. *Infection Immunity* **60** (9), 3918–3920.

SOLER, L., MAGDANZ, V., FOMIN, V.M., SANCHEZ, S. & SCHMIDT, O.G. 2013 Self-propelled micromotors for cleaning polluted water. *ACS Nano* **7** (11), 9611–9620.

SRIDHAR, V., PODJASKI, F., ALAPAN, Y., KRÖGER, J., GRUNENBERG, L., KISHORE, V., LOTSCH, B.V. & SITTI, M. 2022 Light-driven carbon nitride microswimmers with propulsion in biological and ionic media and responsive on-demand drug delivery. *Sci. Robot.* **7** (62), eabm1421.

TAYLOR, G.I. 1953 Dispersion of soluble matter in solvent flowing slowly through a tube. *Proc. R. Soc. Lond. A* **219** (1137), 186–203.

TAYLOR, G.I. 1954*a* Conditions under which dispersion of a solute in a stream of solvent can be used to measure molecular diffusion. *Proc. R. Soc. Lond. A* **225** (1163), 473–477.

TAYLOR, G.I. 1954*b* The dispersion of matter in turbulent flow through a pipe. *Proc. R. Soc. Lond. A* **223** (1155), 446–468.

TURNER, L., RYU, W.S. & BERG, H.C. 2000 Real-time imaging of fluorescent flagellar filaments. *J. Bacteriol.* **182** (10), 2793–2801.

URSO, M., USSIA, M. & PUMERA, M. 2023 Smart micro- and nanorobots for water purification. *Nat. Rev. Bioengng* **1**, 1–16.

VALANI, R.N., HARDING, B. & STOKES, Y.M. 2024 Active particle motion in Poiseuille flow through rectangular channels. *Phys. Rev. E.* **110** (3), 034603.

VEDEL, SØREN & BRUUS, H. 2012 Transient Taylor–Aris dispersion for time-dependent flows in straight channels. *J. Fluid Mech.* **691**, 95–122.

WALKER, B.J., ISHIMOTO, K., MOREAU, C., GAFFNEY, E.A. & DALWADI, M.P. 2022 Emergent rheotaxis of shape-changing swimmers in Poiseuille flow. *J. Fluid Mech.* **944**, R2.

WANG, B., JIANG, W., CHEN, G. & TAO, L. 2022 Transient dispersion in a channel with crossflow and wall adsorption. *Phys. Rev. Fluids* **7** (7), 074501.

WANG, B., JIANG, W., ZENG, L., WU, Z. & WANG, P. 2025 Taylor–aris dispersion of active particles in oscillatory channel flows. *J. Fluid Mech.* **1021**, A3.

WATSON, E.J. 1983 Diffusion in oscillatory pipe flow. *J. Fluid Mech.* **133**, 233–244.

WOMERSLEY, J.R. 1955 Method for the calculation of velocity, rate of flow and viscous drag in arteries when the pressure gradient is known. *J. Physiol.* **127** (3), 553.

ZENG, H., JIANG, W., WANG, B., ZENG, L., GUAN, M., LI, Z. & CHEN, G. 2024 Transient dispersion of settling gyrotactic microorganisms in an open channel flow. *Phys. Fluids* **36** (9), 091918.

ZIA, R.N. & BRADY, J.F. 2010 Single-particle motion in colloids: force-induced diffusion. *J. Fluid Mech.* **658**, 188–210.

ZÖTTL, A. & STARK, H. 2012 Nonlinear dynamics of a microswimmer in Poiseuille flow. *Phys. Rev. Lett.* **108** (21), 218104.

ZÖTTL, A. & STARK, H. 2013 Periodic and quasiperiodic motion of an elongated microswimmer in Poiseuille flow. *Eur. Phys. J. E* **36**, 1–10.